

1

²A SEARCH FOR LONG-LIVED, CHARGED, SUPERSYMMETRIC PARTICLES
³USING IONIZATION WITH THE ATLAS DETECTOR

4

BRADLEY AXEN

5

September 2016 – Version 0.30

6



⁸ Bradley Axen: *A Search for Long-Lived, Charged, Supersymmetric Particles using*
⁹ *Ionization with the ATLAS Detector*, Subtitle, © September 2016

10

Usually a quotation.

11

Dedicated to.

₁₂ ABSTRACT

₁₃ How to write a good abstract:

₁₄ <https://plg.uwaterloo.ca/~migod/research/beck00PSLA.html>

₁₅ PUBLICATIONS

₁₆ Some ideas and figures have appeared previously in the following publications:

₁₇

₁₈ Put your publications from the thesis here. The packages `multibib` or `bibtopic`
₁₉ etc. can be used to handle multiple different bibliographies in your document.

²¹ ACKNOWLEDGEMENTS

²² Put your acknowledgements here.

²³

²⁴ And potentially a second round.

²⁵

26 CONTENTS

27	I	INTRODUCTION	1
28	1	INTRODUCTION	3
29	II	THEORETICAL CONTEXT	5
30	2	STANDARD MODEL	7
31	2.1	Particles	7
32	2.2	Interactions	8
33	2.3	Limitations	8
34	3	SUPERSYMMETRY	9
35	3.1	Motivation	9
36	3.2	Structure	9
37	3.3	Phenomenology	9
38	4	LONG-LIVED PARTICLES	11
39	4.1	Mechanisms	11
40	4.1.1	Examples in Supersymmetry	11
41	4.2	Phenomenology	11
42	4.2.1	Disimilarities to Prompt Decays	11
43	4.2.2	Characteristic Signatures	11
44	III	EXPERIMENTAL STRUCTURE AND RECONSTRUCTION	13
45	5	THE LARGE HADRON COLLIDER	15
46	5.1	Injection Chain	15
47	5.2	Design and Parameters	15
48	5.3	Luminosity	15
49	6	THE ATLAS DETECTOR	17
50	6.1	Coordinate System	17
51	6.2	Magnetic Field	17
52	6.3	Inner Detector	17
53	6.3.1	Pixel Detector	17
54	6.3.2	Semiconductor Tracker	17
55	6.3.3	Transition Radiation Tracker	17
56	6.4	Calorimetry	17
57	6.4.1	Electromagnetic Calorimeters	17
58	6.4.2	Hadronic Calorimeters	17
59	6.4.3	Forward Calorimeters	17
60	6.5	Muon Spectrometer	17
61	6.6	Trigger	17
62	6.6.1	Trigger Scheme	17
63	6.6.2	Missing Transverse Energy Triggers	17
64	7	EVENT RECONSTRUCTION	19
65	7.1	Tracks and Vertices	19

66	7.1.1	Track Reconstruction	19
67	7.1.2	Vertex Reconstruction	19
68	7.2	Jets	19
69	7.2.1	Topological Clustering	19
70	7.2.2	Jet Energy Scale	19
71	7.2.3	Jet Energy Scale Uncertainties	19
72	7.2.4	Jet Energy Resolution	19
73	7.3	Electrons	19
74	7.3.1	Electron Identification	19
75	7.4	Muons	19
76	7.4.1	Muon Identification	19
77	7.5	Missing Transverse Energy	19
78	IV	CALORIMETER RESPONSE	21
79	8	RESPONSE MEASUREMENT WITH SINGLE HADRONS	23
80	8.1	Dataset and Simulation	24
81	8.1.1	Data Samples	24
82	8.1.2	Simulated Samples	24
83	8.1.3	Event Selection	24
84	8.2	Inclusive Hadron Response	25
85	8.2.1	E/p Distribution	26
86	8.2.2	Zero Fraction	26
87	8.2.3	Neutral Background Subtraction	28
88	8.2.4	Corrected Response	28
89	8.3	Identified Particle Response	34
90	8.3.1	Decay Reconstruction	34
91	8.3.2	Identified Response	35
92	8.3.3	Additional Species in Simulation	37
93	8.4	Summary	38
94	9	JET ENERGY RESPONSE AND UNCERTAINTY	41
95	9.1	Motivation	41
96	9.2	Uncertainty Estimate	41
97	9.3	Summary	44
98	V	SEARCH FOR LONG-LIVED PARTICLES	47
99	10	LONG-LIVED PARTICLES IN ATLAS	49
100	10.1	Overview and Characteristics	49
101	10.2	Simulation	49
102	11	EVENT SELECTION	51
103	11.1	Trigger	52
104	11.2	Kinematics and Isolation	52
105	11.3	Standard Model Rejection	56
106	11.4	Ionization	58
107	11.4.1	Mass Estimation	59
108	11.5	Efficiency	60
109	12	BACKGROUND ESTIMATION	63

110	12.1	Background Sources	63
111	12.2	Prediction Method	64
112	12.3	Validation	65
113	12.3.1	Closure in Simulation	65
114	12.3.2	Validation Region in Data	65
115	13	SYSTEMATIC UNCERTAINTIES AND RESULTS	67
116	13.1	Systematic Uncertainties	67
117	13.2	Final Yields	67
118	14	INTERPRETATION	69
119	14.1	Cross Sectional Limits	69
120	14.2	Mass Limits	69
121	14.3	Context for Long-Lived Searches	69
122	VI	CONCLUSIONS	71
123	15	SUMMARY AND OUTLOOK	73
124	15.1	Summary	73
125	15.2	Outlook	73
126	VII	APPENDIX	75
127	A	INELASTIC CROSS SECTION	77
128	B	APPENDIX TEST	79
129	B.1	Appendix Section Test	79
130	B.1.1	Appendix Subection Test	79
131	B.2	A Table and Listing	79
132	B.3	Some Formulas	80
133	BIBLIOGRAPHY		83

134 LIST OF FIGURES

135	Figure 1	The particle content of the Standard Model (SM).	8
136	Figure 2	An illustration (a) of the E/p variable used throughout this paper. The red energy deposits come from the charged particle targeted for measurement, while the blue energy deposits are from nearby neutral particles and must be subtracted. The same diagram (b) for the neutral-background selection, described in Section 8.2.3.	25
137			
138			
139			
140			
141			
142	Figure 3	The E/p distribution and ratio of simulation to data for isolated tracks with (a) $ \eta < 0.6$ and $1.2 < p/\text{GeV} < 1.8$ and (b) $ \eta < 0.6$ and $2.2 < p/\text{GeV} < 2.8$	26
143			
144			
145	Figure 4	The fraction of tracks as a function (a, b) of momentum, (c, d) of interaction lengths with $E \leq 0$ for tracks with positive (on the left) and negative (on the right) charge.	27
146			
147			
148			
149	Figure 5	$\langle E/p \rangle_{\text{BG}}$ as a function of the track momentum for tracks with (a) $ \eta < 0.6$, (b) $0.6 < \eta < 1.1$, and as a function of the track pseudorapidity for tracks with (c) $1.2 < p/\text{GeV} < 1.8$, (d) $1.8 < p/\text{GeV} < 2.2$	29
150			
151			
152			
153	Figure 6	$\langle E/p \rangle_{\text{COR}}$ as a function of track momentum, for tracks with (a) $ \eta < 0.6$, (b) $0.6 < \eta < 1.1$, (c) $1.8 < \eta < 1.9$, and (d) $1.9 < \eta < 2.3$	30
154			
155			
156	Figure 7	$\langle E/p \rangle_{\text{COR}}$ calculated using LCW-calibrated topological clusters as a function of track momentum for tracks with (a) zero or more associated topological clusters or (b) one or more associated topological clusters.	31
157			
158			
159			
160	Figure 8	Comparison of the $\langle E/p \rangle_{\text{COR}}$ for tracks with (a) less than and (b) greater than 20 hits in the TRT.	32
161			
162	Figure 9	Comparison of the $\langle E/p \rangle_{\text{COR}}$ for (a) positive and (b) negative tracks as a function of track momentum for tracks with $ \eta < 0.6$	32
163			
164			
165	Figure 10	Comparison of the E/p distributions for (a) positive and (b) negative tracks with $0.8 < p/\text{GeV} < 1.2$ and $ \eta < 0.6$, in simulation with the FTFP_BERT and QGSP_BERT physics lists.	33
166			
167			
168			
169	Figure 11	Comparison of the response of the hadronic calorimeter as a function of track momentum (a) at the EM-scale and (b) after the LCW calibration.	33
170			
171			
172	Figure 12	Comparison of the response of the EM calorimeter as a function of track momentum (a) at the EM-scale and (b) with the LCW calibration.	34
173			
174			

175	Figure 13	The reconstructed mass peaks of (a) K_S^0 , (b) Λ , and (c) $\bar{\Lambda}$ candidates.	35
176			
177	Figure 14	The E/p distribution for isolated (a) π^+ , (b) π^- , (c) proton, and (d) anti-proton tracks.	36
178			
179	Figure 15	The fraction of tracks with $E \leq 0$ for identified (a) π^+ and π^- , and (b) proton and anti-proton tracks	36
180			
181	Figure 16	The difference in $\langle E/p \rangle$ between (a) π^+ and π^- (b) p and π^+ , and (c) \bar{p} and π^-	37
182			
183	Figure 17	$\langle E/p \rangle_{\text{COR}}$ as a function of track momentum for (a) π^+ tracks and (b) π^- tracks.	38
184			
185	Figure 18	The ratio of the calorimeter response to single parti- cles of various species to the calorimeter response to π^+ with the physics list FTFP_BERT.	38
186			
187	Figure 19	The spectra of true particles inside anti- k_t , $R = 0.4$ jets with (a) $90 < p_T/\text{GeV} < 100$, (b) $400 < p_T/\text{GeV} <$ 500 , and (c) $1800 < p_T/\text{GeV} < 2300$	42
188			
189	Figure 20	The jet energy scale (JES) uncertainty contributions, as well as the total JES uncertainty, as a function of jet p_T for (a) $ \eta < 0.6$ and (b) $0.6 < \eta < 1.1$	44
190			
191	Figure 21	The JES correlations as a function of jet p_T and $ \eta $ for jets in the central region of the detector.	45
192			
193	Figure 22	The distribution of E_T^{miss} for data and simulated signal events, after the trigger requirement.	53
194			
195	Figure 23	The dependence of dE/dx on N_{split} in data after basic track hit requirements have been applied.	54
196			
197	Figure 24	The distribution of dE/dx with various selections ap- plied in data and simulated signal events.	55
198			
199	Figure 25	The distribution of track momentum for data and sim- ulated signal events, after previous selection require- ments have been applied.	55
200			
201	Figure 26	The distribution of M_T for data and simulated sig- nal events, after previous selection requirements have been applied.	56
202			
203	Figure 27	The distribution of summed tracked momentum within a cone of $\Delta R < 0.25$ around the candidate track for data and simulated signal events, after previous selec- tion requirements have been applied.	57
204			
205	Figure 28	The normalized, two-dimensional distribution of E/p and f_{EM} for simulated (a) $Z \rightarrow ee$, (b) $Z \rightarrow \tau\tau$, (c) 1200 GeV Stable R-Hadron events, and (d) 1200 GeV, 10 ns R-Hadron events.	58
206			
207	Figure 29	Two-dimensional distribution of dE/dx versus charge signed momentum (qp) for minimum-bias tracks. The fitted distributions of the most probable values for pi- ons, kaons and protons are superimposed.	59
208			
209			
210			
211			
212			
213			
214			
215			
216			
217			
218			
219			

220	Figure 30	The distribution of mass estimated using dE/dx for simulated stable R-Hadrons with masses between 1000 and 1600 GeV.	60
221			
222			
223	Figure 31	The acceptance \times efficiency as a function of R-Hadron (a) mass and (b) lifetime. (a) shows all of the combinations of mass and lifetime considered in this search, and (b) highlights the lifetime dependence for 1000 GeV and 1600 GeV R-Hadrons.	62
224			
225			
226			
227			
228	Figure 32	The distribution of (a) dE/dx and (b) momentum for tracks in data and simulated signal after requiring the event level selection and the track selection on p_T , hits, and N_{split} . Each subfigure shows the normalized distributions for tracks classified as hadrons, electrons, and muons in data and R-Hadrons in the simulated signal.	64
229			
230			
231			
232			
233			
234			

235 LIST OF TABLES

247 LISTINGS

<small>248</small>	Listing 1	A floating example (<code>listings</code> manual)	80
--------------------	-----------	--	----

²⁴⁹ ACRONYMS

- ²⁵⁰ SM Standard Model
- ²⁵¹ LSP Lightest Supersymmetric Particle
- ²⁵² LHC Large Hadron Collider
- ²⁵³ ToT time over threshold
- ²⁵⁴ LCW local cluster weighted
- ²⁵⁵ MIP minimally ionizing particle
- ²⁵⁶ EPJC European Physical Journal C
- ²⁵⁷ JES jet energy scale
- ²⁵⁸ LLP Long-Lived Particle
- ²⁵⁹ CR Control Region

260

PART I

261

INTRODUCTION

262

You can put some informational part preamble text here.

1

263

264 INTRODUCTION

265

PART II

266

THEORETICAL CONTEXT

267

You can put some informational part preamble text here.

2

268

269 STANDARD MODEL

270 The SM of particle physics seeks to explain the symmetries and interactions of
271 all currently discovered fundamental particles. It has been tested by several genera-
272 tions of experiments and has been remarkably successful, no significant de-
273 viations have been found. The SM provides predictions in particle physics for
274 interactions up to the Planck scale (10^{15} - 10^{19} GeV).

275 The theory itself is a quantum field theory grown from an underlying $SU(3) \times$
276 $SU(2) \times U(1)$ that requires the particle content and quantum numbers consist-
277 ent with experimental observations (see Section 2.1). Each postulated symme-
278 try is accompanied by an interaction between particles through gauge invari-
279 ance. These interactions are referred to as the Strong, Weak, and Electromag-
280 netic forces, which are discussed in Section 2.2.

281 Although this model has been very predictive, the theory is incomplete; for
282 example, it is not able to describe gravity or astronomically observed dark matter.
283 These limitations are discussed in more detail in Section 2.3.

284 21 PARTICLES

285 The most familiar matter in the universe is made up of protons, neutrons, and
286 electrons. Protons and neutrons are composite particles, however, and are made
287 up in turn by particles called quarks. Quarks carry both electric charge and color
288 charge, and are bound in color-neutral combinations called baryons. The elec-
289 tron is an example of a lepton, and carries only electric charge. Another type
290 of particle, the neutrino, does not form atomic structures in the same way that
291 quarks and leptons do because it carries no color or electric charge. Collectively,
292 these types of particles are known as fermions, the group of particles with half-
293 integer spin.

294 There are three generations of fermions, although familiar matter is formed
295 predominantly by the first generation. The generations are identical except for
296 their masses, which increase in each generation by convention. In addition, each
297 of these particles is accompanied by an antiparticle, with opposite-sign quantum
298 numbers but the same mass.

299 The fermions comprise what is typically considered matter, but there are
300 additional particles that are mediators of interactions between those fermions.
301 These mediators are known as the gauge bosons, gauge in that their existence
302 is required by gauge invariance (discussed further in Section 2.2) and bosons in
303 that they have integer spin. The boson which mediates the electromagnetic force
304 is the photon, the first boson to be discovered; it has no electric charge, no mass,
305 and a spin of 1. There are three spin-1 mediators of the weak force, the two
306 W bosons and the Z boson. The W bosons have electric charge of ± 1 and a
307 mass of 80.385 ± 0.015 GeV, while the Z boson is neutral and has a mass of

308 91.1876 \pm 0.0021 GeV. The strong force is mediated by eight particles called
 309 gluons, which are massless and electrically neutral but do carry color charge.

310 The final particle present in the SM is the Higgs boson, which was recently
 311 observed for the first time by experiments at CERN in 2012. It is electrically
 312 neutral, has a mass of 125.7 \pm 0.4 GeV, and is the only spin-0 particle yet to be
 313 observed. The Higgs boson is the gauge boson associated with the mechanism
 314 that gives a mass to the W and Z bosons.

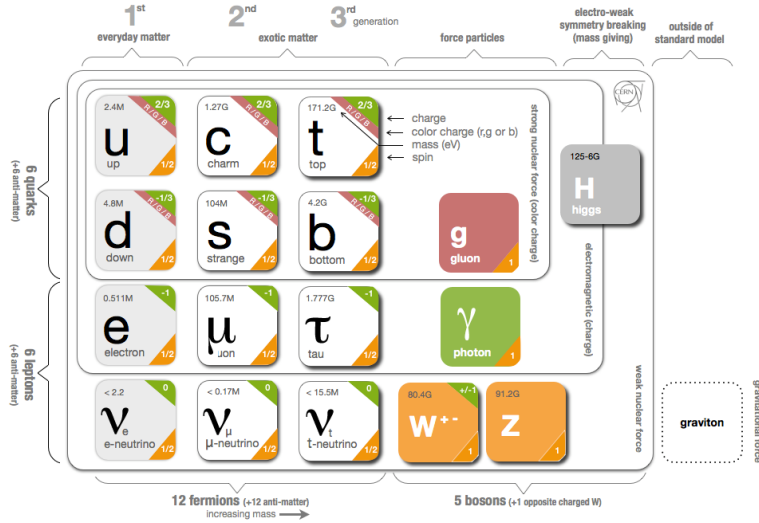


Figure 1: The particle content of the SM.

315 Together these particles form the entire content of the SM, and are summa-
 316 rized in Figure 1. These are the particles that constitute the observable universe
 317 and all the so-far-observed interactions within it.

318 2.2 INTERACTIONS

319 The interactions predicted and described by the SM are fundamentally tied to the
 320 particles within it, both in that they describe the way those particles can influence
 321 each other and also in that the existence of the interactions requires the existence
 322 of some particles (the gauge bosons).

323 2.3 LIMITATIONS

3

324

325 SUPERSYMMETRY

326 3.1 MOTIVATION

327 3.2 STRUCTURE

328 3.3 PHENOMENOLOGY

4

329

330 LONG-LIVED PARTICLES

331 4.1 MECHANISMS

332 4.1.1 EXAMPLES IN SUPERSYMMETRY

333 4.2 PHENOMENOLOGY

334 4.2.1 DISIMILARITIES TO PROMPT DECAYS

335 4.2.2 CHARACTERISTIC SIGNATURES

336

PART III

337

EXPERIMENTAL STRUCTURE AND RECONSTRUCTION

338

You can put some informational part preamble text here.

5

339

340 THE LARGE HADRON COLLIDER

341 5.1 INJECTION CHAIN

342 5.2 DESIGN AND PARAMETERS

343 5.3 LUMINOSITY

6

344

345 THE ATLAS DETECTOR

346 6.1 COORDINATE SYSTEM

347 6.2 MAGNETIC FIELD

348 6.3 INNER DETECTOR

349 6.3.1 PIXEL DETECTOR

350 6.3.2 SEMICONDUCTOR TRACKER

351 6.3.3 TRANSITION RADIATION TRACKER

352 6.4 CALORIMETRY

353 6.4.1 ELECTROMAGNETIC CALORIMETERS

354 6.4.2 HADRONIC CALORIMETERS

355 6.4.3 FORWARD CALORIMETERS

356 6.5 MUON SPECTROMETER

357 6.6 TRIGGER

358 6.6.1 TRIGGER SCHEME

359 6.6.2 MISSING TRANSVERSE ENERGY TRIGGERS

7

360

361 EVENT RECONSTRUCTION

362 The ATLAS experiment combines measurements in the subdetectors to form a
363 cohesive picture of each physics event.

364 7.1 TRACKS AND VERTICES

365 7.1.1 TRACK RECONSTRUCTION

366 7.1.1.1 NEURAL NETWORK

367 7.1.1.2 PIXEL DE/DX

368 7.1.2 VERTEX RECONSTRUCTION

369 7.2 JETS

370 7.2.1 TOPOLOGICAL CLUSTERING

371 7.2.2 JET ENERGY SCALE

372 7.2.3 JET ENERGY SCALE UNCERTAINTIES

373 7.2.4 JET ENERGY RESOLUTION

374 7.3 ELECTRONS

375 7.3.1 ELECTRON IDENTIFICATION

376 7.4 MUONS

377 7.4.1 MUON IDENTIFICATION

378 7.5 MISSING TRANSVERSE ENERGY

379

PART IV

380

CALORIMETER RESPONSE

381

You can put some informational part preamble text here.

382

383 RESPONSE MEASUREMENT WITH SINGLE HADRONS

384 As discussed in Section 7.2, colored particles produced in collisions hadronize
385 into jets of multiple hadrons. One approach to understanding jet energy mea-
386 surements in the ATLAS calorimeters is to evaluate the calorimeter response to
387 those individual hadrons; measurements of individual hadrons can be used to
388 build up an understanding of the jets that they form. The redundancy of the
389 momentum provided by the tracking system and the energy provided by the
390 calorimeter provides an opportunity to study calorimeter response using real
391 collisions, as described further in Section 8.2.

392 Calorimeter response includes a number of physical effects that can be ex-
393 tracted to provide insight into many aspects of jet modeling. First, many charged
394 hadrons interact with the material of the detector prior to reaching the calorime-
395 ters and thus do not deposit any energy. Comparing this effect in data and simu-
396 lation is a powerful tool in validating the interactions of particles with the mate-
397 rial of the detector and the model of the detector geometry in simulation, see Sec-
398 tion 8.2.2. The particles which do reach the calorimeter deposit their energy into
399 several adjacent cells, which are then clustered together. The energy of the clus-
400 ter is then the total energy deposited by that particle. Comparing the response of
401 hadrons in data to that of simulated hadrons provides a direct evaluation of the
402 showering of hadronic particles and the energy deposited by particles in matter
403 (Section 8.2.4).

404 The above studies all use an inclusive selection of charged particles, which are
405 comprised predominantly of pions, kaons, and (anti)protons. It is also possible to
406 measure the response to various identified particle types separately to evaluate
407 the simulated interactions of each particle, particularly at low energies where
408 differences between species are very relevant. Pions and (anti)protons can be
409 identified through decays of long-lived particles, in particular Λ , $\bar{\Lambda}$, and K_S^0 , and
410 then used to measure response as described above. This is discussed in detail in
411 Section 8.3.

412 Together, these measurements in data provide a thorough understanding of
413 the way hadrons interact with the ATLAS detector and can be used to build up a
414 description of jets, as seen in Chapter 9. The results in this chapter use data col-
415 lected at 7 and 8 TeV collected in 2010 and 2012, respectively. Both are included
416 as the calorimeter was repaired and recalibrated between those two data-taking
417 periods. Both sets of data are compared to an updated simulation that includes
418 new physics models provided by Geant4 [1] and improvements in the detec-
419 tor description [2, 3]. These results are published in European Physical Journal
420 C (EPJC) [4] and can be compared to a similar measurement performed in 2009
421 and 2010 [5], which used the previous version of the simulation framework [6].

422 8.1 DATASET AND SIMULATION

423 8.1.1 DATA SAMPLES

424 The two datasets used in this chapter are taken from dedicated low-pileup runs
 425 where the fraction of events with multiple interactions was negligible, to facilitate
 426 measurement of isolated hadrons. The 2012 dataset at $\sqrt{s} = 8$ TeV contains
 427 8 million events and corresponds to an integrated luminosity of 0.1 nb^{-1} . The
 428 2010 dataset at $\sqrt{s} = 7$ TeV contains 3 million events and corresponds to an
 429 integrated luminosity of 3.2 nb^{-1} . The latter dataset was also used in the 2010
 430 results [5], but it has since been reanalyzed with an updated detector description
 431 for the material and alignment.

432 8.1.2 SIMULATED SAMPLES

433 The two datasets above are compared to simulated single-, double-, and non-
 434 diffractive events generated with Pythia8 [7] using the A2 configuration of
 435 hadronization [8] and the MSTW 2008 parton-distribution function set [9, 10].
 436 The conditions and energies for each run are matched in the two simulations.

437 To evaluate the interaction of hadrons with detector material, the simulation
 438 uses two different collections of hadronic physics models, called physics lists, in
 439 Geant4 9.4 [11]. The first, QGSP_BERT, combines the Bertini intra-nuclear
 440 cascade [12–14] below 9.9 GeV, a parametrized proton inelastic model from 9.5
 441 to 25 GeV [15], and a quark-gluon string model above 12 GeV [16–20]. The
 442 second, FTFP_BERT, combines the Bertini intra-nuclear cascade [12–14] below
 443 5 GeV and the Fritiof model [21–24] above 4 GeV. In either list, Geant4 en-
 444 forces a smooth transition between models where multiple models overlap.

445 8.1.3 EVENT SELECTION

446 The event selection for this study is minimal, as the only requirement is selecting
 447 good-quality events with an isolated track. Such events are triggered by requir-
 448 ing at least two hits in the minimum-bias trigger scintillators. After trigger, each
 449 event is required to have exactly one reconstructed vertex, and that vertex is re-
 450 quired to have four or more associated tracks.

451 The particles which enter into the response measurements are first identified
 452 as tracks in the inner detector. The tracks are required to have at least 500 MeV
 453 of transverse momentum. To ensure a reliable momentum measurement, these
 454 tracks are required to have at least one hit in the pixel detector, six hits in the SCT,
 455 and small longitudinal and transverse impact parameters with respect to the pri-
 456 mary vertex [5]. For the majority of the measurements in this chapter, the track is
 457 additionally required to have 20 hits in the TRT, which significantly reduces the
 458 contribution from tracks which undergo nuclear interactions. This requirement
 459 and its effect is discussed in more detail in Section 8.2.4.1. In addition, tracks are
 460 rejected if there is another track which extrapolates to the calorimeter within a

cone of $\Delta R = \sqrt{(\Delta\phi)^2 + (\Delta\eta)^2} < 0.4$. This requirement guarantees that the contamination of energy from nearby charged particles is negligible [5].

8.2 INCLUSIVE HADRON RESPONSE

The calorimeter response is more precisely defined as the ratio of the measured calorimeter energy to the true energy carried by the particle, although this true energy is unknown. For charged particles, however, the inner detector provides a very precise measurement of momentum (with uncertainty less than 1%) that can be used as a proxy for true energy. The ratio of the energy deposited by the charged particle in the calorimeter, E , to its momentum measured in the inner detector p , forms the calorimeter response measure called E/p . Though the distribution of E/p contains a number of physical features, this study focuses on the trends in two aggregated quantities: $\langle E/p \rangle$, the average of E/p within a given subset of particles, and the zero fraction, the fraction of particles with no associated energy in the calorimeter.

The calorimeter energy assigned to a track particle is defined using clusters. The clusters are formed using a 4–2–0 algorithm [25] that begins with seeds requiring at least 4 times the average calorimeter noise. The neighboring cells with at least twice that noise threshold are then added to the cluster, and all bounding cells are then added with no requirement. This algorithm minimizes noise contributions through its seeding process, and including the additional layers improves the energy resolution [26]. The clusters are associated to a given track if they fall within a cone of $\Delta R = 0.2$ of the extrapolated position of the track, which includes about 90% of the energy on average [5]. This construction is illustrated in Figure 2.

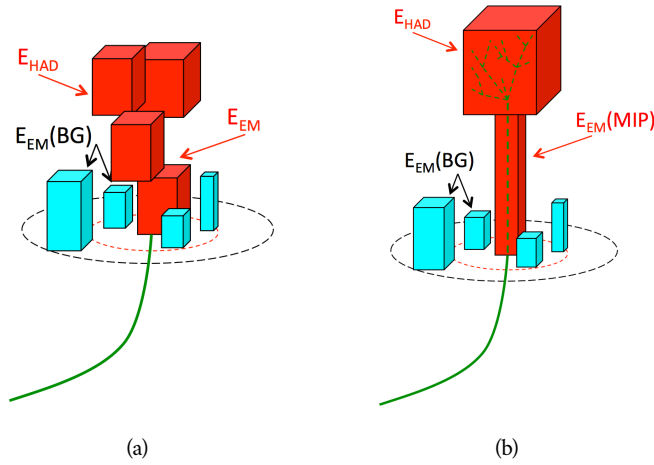


Figure 2: An illustration (a) of the E/p variable used throughout this paper. The red energy deposits come from the charged particle targeted for measurement, while the blue energy deposits are from nearby neutral particles and must be subtracted. The same diagram (b) for the neutral-background selection, described in Section 8.2.3.

485 8.2.1 E/P DISTRIBUTION

486 The E/p distributions measured in both data and simulation are shown in Figure 3 for two example bins of track momentum and for tracks in the central
 487 region of the detector. These distributions show several important features of
 488 the E/p observable. The large content in the bin at $E = 0$ comes from tracks
 489 that have no associated cluster, which occurs due to interactions with detector
 490 material prior to reaching the calorimeter or the energy deposit being insuffi-
 491 ciently large to generate a seed, and are discussed in Section 8.2.2. The small
 492 negative tail comes from similar tracks that do not deposit any energy in the
 493 calorimeter but are randomly associated to a noise cluster. The long positive
 494 tail above 1.0 comes from the contribution of neutral particles. Nearby neutral
 495 particles deposit (sometimes large) additional energy in the calorimeter but do
 496 not produce tracks in the inner detector, so they cannot be rejected by the track
 497 isolation requirement. Additionally the peak and mean of the distribution falls
 498 below 1.0 because of the loss of energy not found within the cone as well as the
 499 non-compensation of the calorimeter.
 500

501 The data and simulation share the same features, but the high and low tails
 502 are significantly different. The simulated events tend to overestimate the con-
 503 tribution of neutral particles to the long tail, an effect which can be isolated and
 504 removed as discussed in Section 8.2.3. Additionally, the simulated clusters have
 505 less noise on average, although this is a small effect on the overall response.

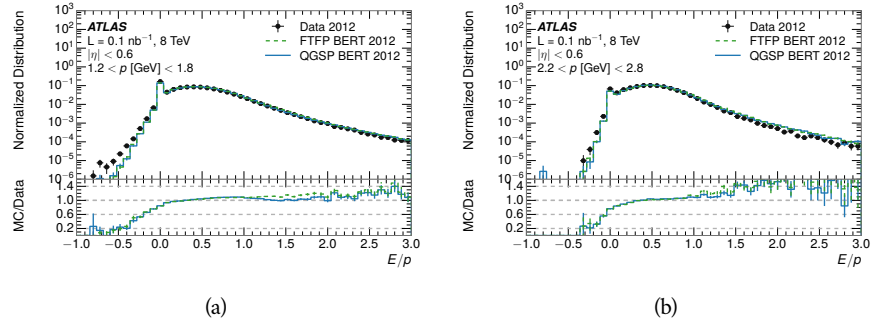


Figure 3: The E/p distribution and ratio of simulation to data for isolated tracks with
 (a) $|\eta| < 0.6$ and $1.2 < p/\text{GeV} < 1.8$ and (b) $|\eta| < 0.6$ and $2.2 < p/\text{GeV} < 2.8$.

506 8.2.2 ZERO FRACTION

507 The fraction of particles with no associated clusters, or similarly those with $E \leq$
 508 0, reflects the modeling of both the detector geometry and hadronic interactions.
 509 The zero fraction is expected to rise as the amount of material a particle traverses
 510 increases, while it is expected to decrease as the particle energy increases. This
 511 dependence can be seen in Figure 4, where the zero fraction in data and simula-
 512 tion is shown as a function of momentum and the amount of material measured
 513 in interaction lengths. The trends are similar between the 2010 and 2012 mea-
 514 surements. The zero fraction decreases with energy as expected. The amount of

material in the detector increases with η , which provides a distribution of interaction lengths. As the data and simulation have significant disagreement in the zero fraction over a number of interaction lengths, the difference must be primarily from the modeling of hadronic interactions with detector material and not just the detector geometry.

There is also a noticeable difference between positive and negative tracks at low momentum, which reflects the difference in response between protons and antiprotons. Antiprotons have significant model differences in the two physics lists, QGSP_BERT and FTFP_BERT, and this is evident in the lowest momentum bin of the data to simulation ratio. This difference is explored further in Section 8.3.

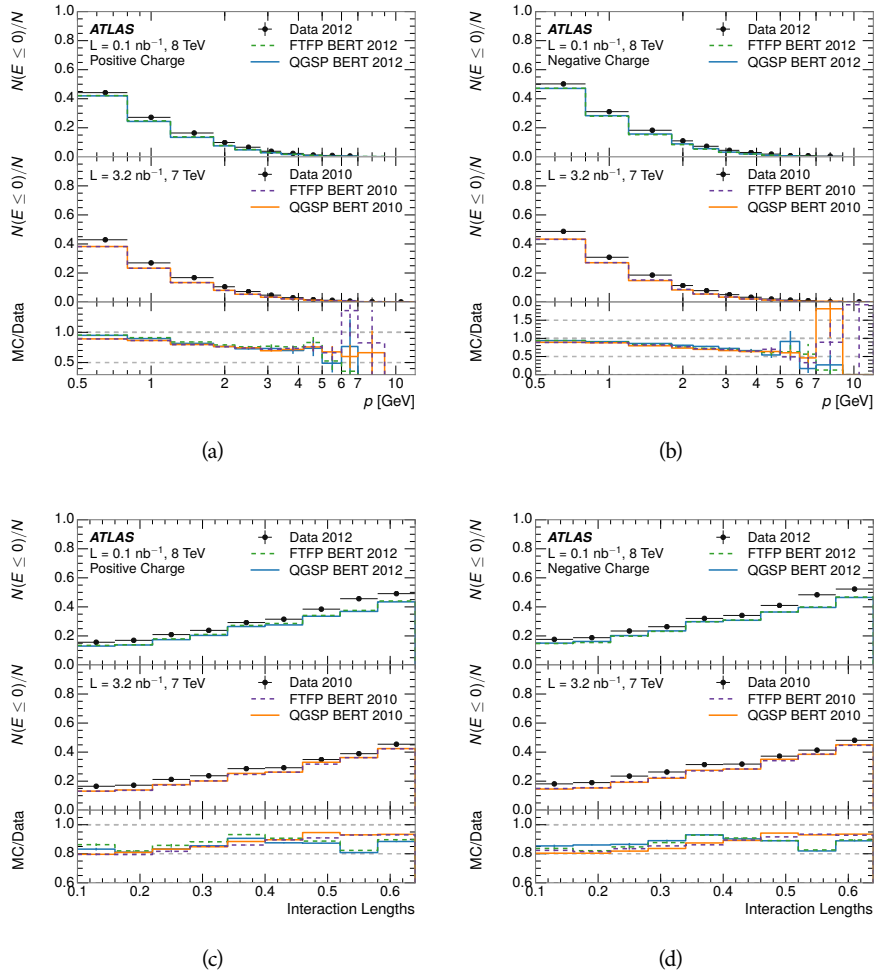


Figure 4: The fraction of tracks as a function (a, b) of momentum, (c, d) of interaction lengths with $E \leq 0$ for tracks with positive (on the left) and negative (on the right) charge.

526 8.2.3 NEUTRAL BACKGROUND SUBTRACTION

527 The isolation requirement on hadrons is only effective in remove energy contri-
 528 bution from nearby charged particles. Nearby neutral particles, predominantly
 529 photons from π^0 decays, also add their energy to the calorimeter clusters, but
 530 mostly in the electromagnetic calorimeter. It is possible to measure this contri-
 531 bution, on average, using late-showering hadrons that minimally ionize in the
 532 electromagnetic calorimeter. Such particles are selected by requiring that they
 533 deposit less than 1.1 GeV in the EM calorimeter within a cone of $\Delta R < 0.1$
 534 around the track. To ensure that these particles are well measured, they are addi-
 535 tionally required to deposit between 40% and 90% of their energy in the hadronic
 536 calorimeter within the same cone.

537 These particles provide a clean sample to measure the nearby neutral back-
 538 ground because they do not deposit energy in the area immediately surrounding
 539 them in the EM calorimeter, as shown in Figure 2. So, the energy deposits in the
 540 region $0.1 < \Delta R < 0.2$ can be attributed to neutral particles alone. To estimate
 541 the contribution to the whole cone considered for the response measurement,
 542 that energy is scaled by a geometric factor of 4/3. This quantity, $\langle E/p \rangle_{\text{BG}}$, mea-
 543 sured in aggregate over a number of particles, gives the contribution to $\langle E/p \rangle$
 544 from neutral particles in the EM calorimeter. Similar techniques were used in
 545 the individual layers of the hadronic calorimeters to show that the background
 546 from neutrals is negligible in those layers [5].

547 The distribution of this background estimate is shown in Figure 5. Although
 548 the simulation captures the overall trend, it significantly overestimates the neu-
 549 tral contribution for tracks with momentum between 2 and 8 GeV. This effect
 550 was also seen in the tails of the E/p distributions in Figure 3. This difference is
 551 likely due to the modeling of coherent neutral particle radiation in Pythia8, as
 552 the discrepancy does not depend on η and thus is unlikely to be a mismodeling
 553 of the detector. This difference can be subtracted to form a corrected average
 554 E/p , as in Section 8.2.4.

555 8.2.4 CORRECTED RESPONSE

556 Figure 6 shows $\langle E/p \rangle_{\text{COR}}$ as a function of momentum for several bins of pseu-
 557 dorapidity. This corrected $\langle E/p \rangle_{\text{COR}} \equiv \langle E/p \rangle - \langle E/p \rangle_{\text{BG}}$ measures the average
 558 calorimeter response without the contamination of neutral particles. It is the
 559 most direct measurement of calorimeter response in that it is the energy mea-
 560 sured for fully isolated hadrons. The correction is performed separately in data
 561 and simulation, so that the mismodeling of the neutral background in simulation
 562 is removed from the comparison of response. The simulation overestimates the
 563 response at low momentum by about 5%, an effect that can be mostly attributed
 564 to the underestimation of the zero fraction mentioned previously.

565 The response measurement above used topological clustering at the EM scale,
 566 that is clusters were formed to measure energy but no corrections were applied
 567 to correct for expected effects like energy lost outside of the cluster or in unin-
 568 strumented material. It is also interesting to measure $\langle E/p \rangle_{\text{COR}}$ using local clus-

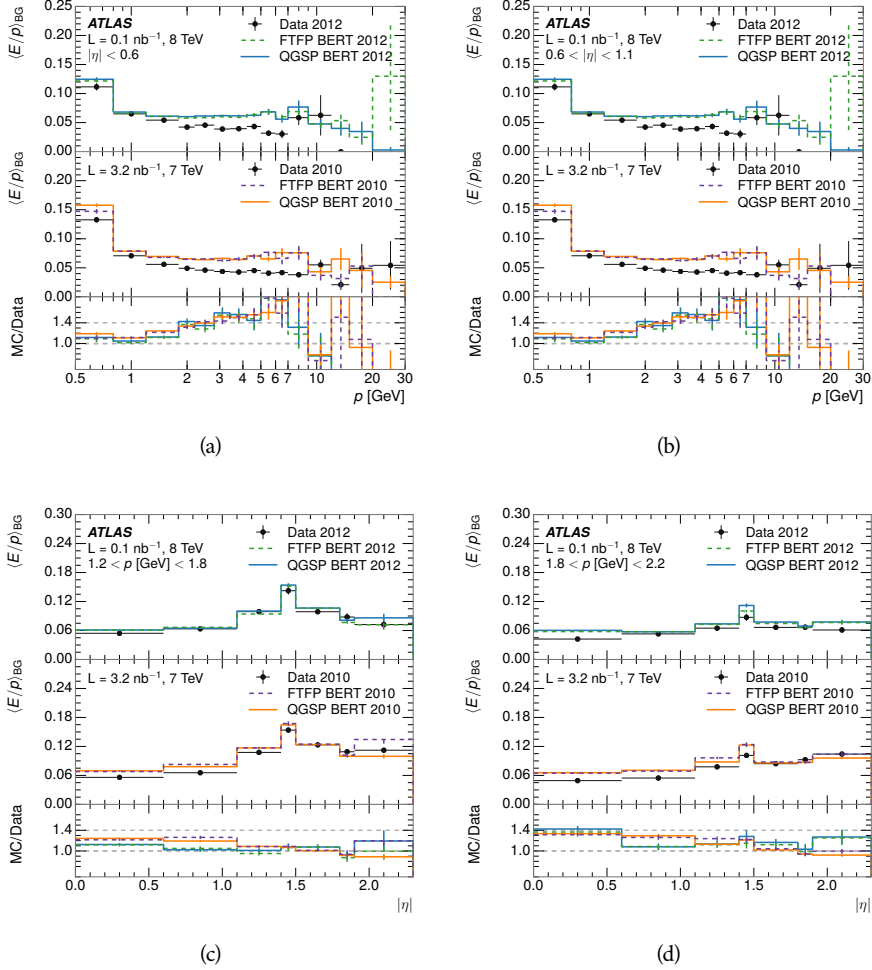


Figure 5: $\langle E/p \rangle_{\text{BG}}$ as a function of the track momentum for tracks with (a) $|\eta| < 0.6$, (b) $0.6 < |\eta| < 1.1$, and as a function of the track pseudorapidity for tracks with (c) $1.2 < p/\text{GeV} < 1.8$, (d) $1.8 < p/\text{GeV} < 2.2$.

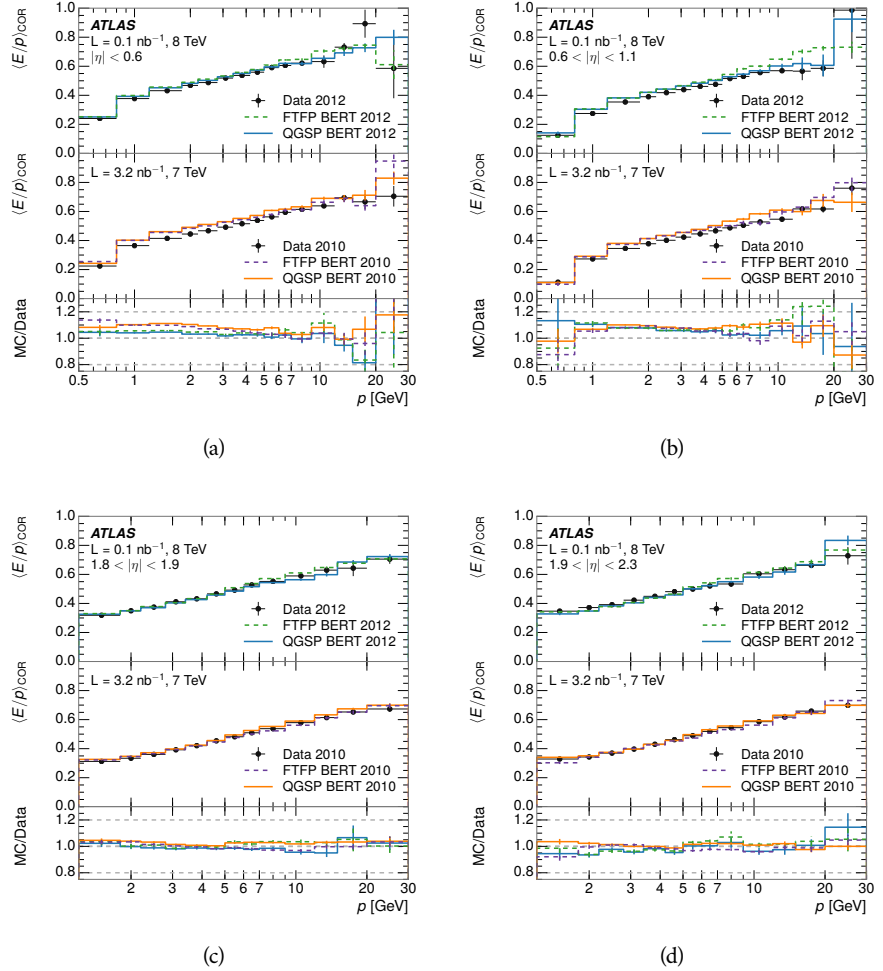


Figure 6: $\langle E/p \rangle_{\text{COR}}$ as a function of track momentum, for tracks with (a) $|\eta| < 0.6$, (b) $0.6 < |\eta| < 1.1$, (c) $1.8 < |\eta| < 1.9$, and (d) $1.9 < |\eta| < 2.3$.

569 ter weighted (LCW) energies, which accounts for those effects by calibrating the
 570 energy based on the properties of the cluster such as energy density and depth in
 571 the calorimeter. Figure 7 shows these distributions for tracks with zero or more
 572 clusters and separately for tracks with one or more clusters. The calibration
 573 moves $\langle E/p \rangle_{\text{COR}}$ significantly closer to 1.0, which is the purpose of the calibra-
 574 tion. The agreement between data and simulation improves noticeably when at
 575 least one cluster is required, as this removes the contribution from the mismod-
 576 eling of the zero fraction.

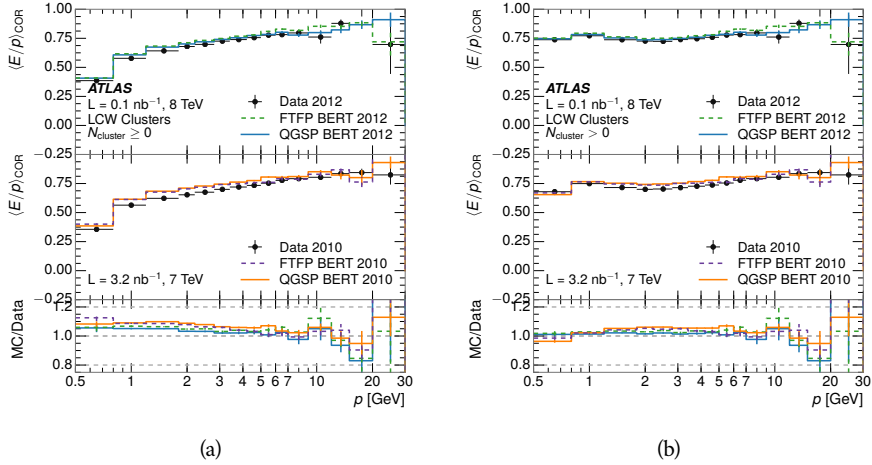


Figure 7: $\langle E/p \rangle_{\text{COR}}$ calculated using LCW-calibrated topological clusters as a function of track momentum for tracks with (a) zero or more associated topological clusters or (b) one or more associated topological clusters.

577 8.2.41 ADDITIONAL STUDIES

578 As has been seen in several previous measurements, the simulation does not
 579 correctly model the chance of a low momentum hadron to reach the calorime-
 580 ter. Because of the consistent discrepancy across pseudorapidity and interaction
 581 lengths, this seems to be best explained by incomplete understanding of hadronic
 582 interactions with the detector. For example, a hadron that scatters off of a nu-
 583 cleus in the inner detector can be deflected through a significant angle and not
 584 reach the expected location in the calorimeter. In addition, these interactions
 585 can produce secondary particles that are difficult to model.

586 The requirement on the number of hits in the TRT reduces these effects by
 587 preferentially selecting tracks that do not undergo nuclear interactions. It is inter-
 588 esting to check how well the simulation models tracks with low numbers of
 589 TRT hits, where the nuclear interactions are much more likely. Figure 8 com-
 590 pares the distributions with $N_{\text{TRT}} < 20$ to $N_{\text{TRT}} > 20$ for real and simulated
 591 particles. As expected, the tracks with fewer hits are poorly modeled in the sim-
 592 ulation as $\langle E/p \rangle_{\text{COR}}$ differs by as much as 25% at low momentum.

593 Another interesting aspect of the simulation is the description of antiprotons
 594 at low momentum, where QGSP_BERT and FTFP_BERT have significant differ-
 595 ences. This can be seen to have an effect in the inclusive response measurement

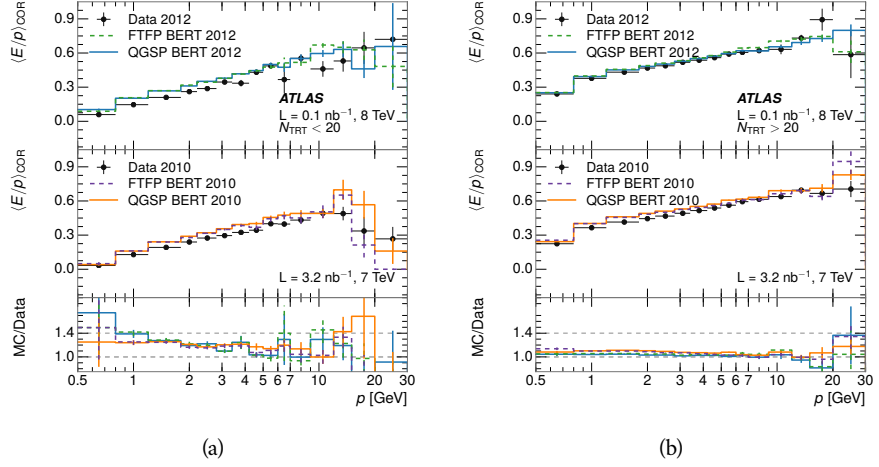


Figure 8: Comparison of the $\langle E/p \rangle_{\text{COR}}$ for tracks with (a) less than and (b) greater than 20 hits in the TRT.

when separated into positive and negative charge. The $\langle E/p \rangle_{\text{COR}}$ distributions for positive and negative particles are shown in Figure 9, where a small difference between QGSP_BERT and FTFP_BERT can be seen in the distribution for negative tracks. This is demonstrated more clearly in Figure 10, which shows the E/p distribution in the two simulations separated by charge. There is a clear difference around $E/p > 1.0$, which can be explained by the additional energy deposited by the annihilation of the antiproton in the calorimeter that is modeled well only in FTFP_BERT. This is also explored with data using identified antiprotons in Section 8.3.

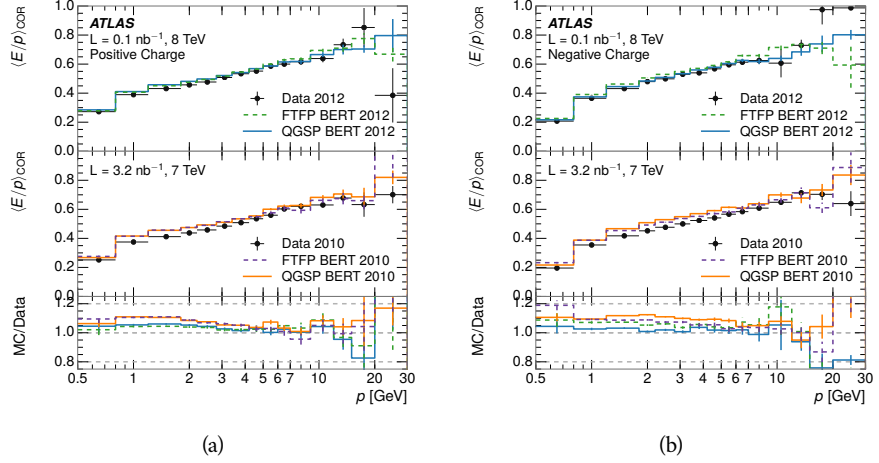


Figure 9: Comparison of the $\langle E/p \rangle_{\text{COR}}$ for (a) positive and (b) negative tracks as a function of track momentum for tracks with $|\eta| < 0.6$.

The $\langle E/p \rangle$ results in previous sections have considered the electromagnetic and hadronic calorimeters together as a single energy measurement, to emphasize the total energy deposited for a given particle. However, the deposits in each

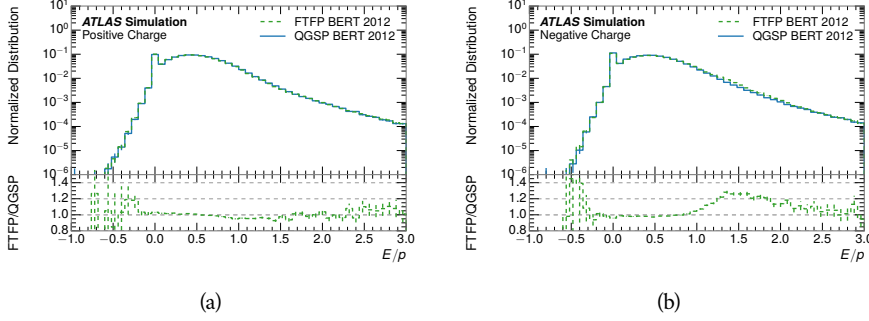


Figure 10: Comparison of the E/p distributions for (a) positive and (b) negative tracks with $0.8 < p/\text{GeV} < 1.2$ and $|\eta| < 0.6$, in simulation with the FTFP_BERT and QGSP_BERT physics lists.

calorimeter are available separately and $\langle E/p \rangle$ can be constructed for each layer. As the layers are composed of different materials and are modeled separately in the detector geometry, confirmation that the simulation matches the data well in each layer adds confidence in both the description of hadronic interactions with the two different materials and also the geometric description of each.

The technique discussed in Section 8.2.3 for selecting minimally ionizing particle (**MIP**s) in the electromagnetic calorimeter is also useful in studying deposits in the hadronic calorimeter. Those **MIP**s deposit almost all of their energy exclusively in the hadronic calorimeter. Figure 11 shows $\langle E/p \rangle_{\text{Had}}^{\text{Had}}$, where RAW indicates that no correction has been applied for neutral backgrounds and Had indicates that only clusters for the hadronic calorimeter are included. The RAW and COR versions of $\langle E/p \rangle$ in this case are the same, as the neutral background is negligible in that calorimeter layer. The distributions are shown both for the original EM scale calibration and after LCW calibration. The data and simulation agree very well in this comparison, except in the lowest momentum bin which has 5% discrepancy that has already been seen in similar measurements.

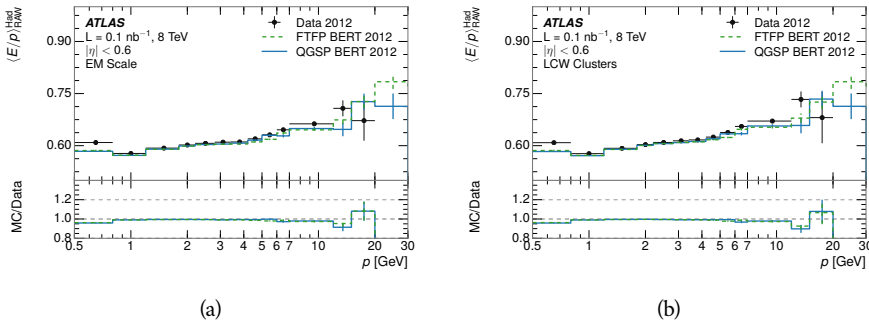


Figure 11: Comparison of the response of the hadronic calorimeter as a function of track momentum (a) at the EM-scale and (b) after the LCW calibration.

A similar comparison can be made in the electromagnetic calorimeter by selecting particles which have no associated energy in the hadronic calorimeter. These results are measured in terms of $\langle E/p \rangle_{\text{COR}}^{\text{EM}}$, where EM designates that

627 only clusters in the electromagnetic calorimeter are included and COR designates
 628 that the neutral background is subtracted as the neutral background is
 629 present in this case. Figure 12 shows the analogous comparisons to Figure 11 in
 630 the electromagnetic calorimeter. In this case the disagreement between data and
 631 simulation is more pronounced, with discrepancies as high as 5% over a larger
 632 range of momenta. This level of discrepancy indicates that the description of
 633 the electromagnetic calorimeter is actually the dominant source of discrepancy
 634 in the combined distributions in Section 8.2.4.

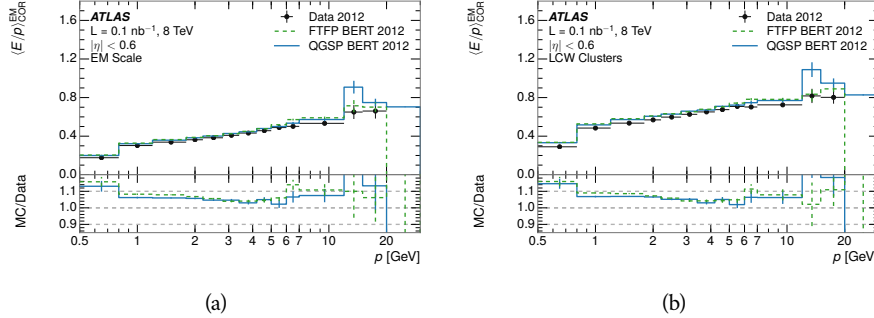


Figure 12: Comparison of the response of the EM calorimeter as a function of track momentum (a) at the EM-scale and (b) with the LCW calibration.

635 **NOTE: There are more studies that I skipped for brevity that could be in-**
 636 **cluded if interesting. E/p at different cluster threshold settings, E/p with**
 637 **pileup, E/p with cells. I also left out a lot of eta bins that appear in the**
 638 **paper so that this section didn't turn into 20 pages of plots.**

639 8.3 IDENTIFIED PARTICLE RESPONSE

640 The inclusive response measurement for hadrons can be augmented by measur-
 641 ing the response for specific particle species. The simulation models each parti-
 642 cle type separately, and understanding the properties of each is important in con-
 643 straining the uncertainty on jets. In order to select and measure specific hadrons,
 644 this section relies on the displaced decays of long-lived particles. Such decays
 645 can be identified by reconstructing secondary vertices with a requirement on
 646 mass. In particular, Λ , $\bar{\Lambda}$, and K_S^0 can be used to select a pure sample of protons,
 647 antiprotons, and pions, respectively.

648 8.3.1 DECAY RECONSTRUCTION

649 The measurement of response for identified particles uses the same selection as
 650 for inclusive particles (Section 8.1.3) with a few additions. Each event used is
 651 required to have at least one secondary vertex, and the tracks are required to
 652 match to that vertex rather than the primary vertex. Pions are selected from
 653 decays of $K_S^0 \rightarrow \pi^+ \pi^-$, which is the dominant decay for K_S^0 to charged particles.
 654 Protons are selected from decays of $\Lambda \rightarrow \pi^- p$ and antiprotons from $\bar{\Lambda} \rightarrow \pi^+ \bar{p}$,

which are similarly the dominant decays of Λ and $\bar{\Lambda}$ to charged particles. The species of parent hadron in these decays is determined by reconstructing the mass of the tracks associated to the secondary vertex. The sign of the higher momentum decay particle can distinguish between Λ and $\bar{\Lambda}$, which of course have the same mass, as the proton or antiproton is kinematically favored to have higher momentum. Examples of the reconstructed masses used to select these decays are shown in Figure 13.

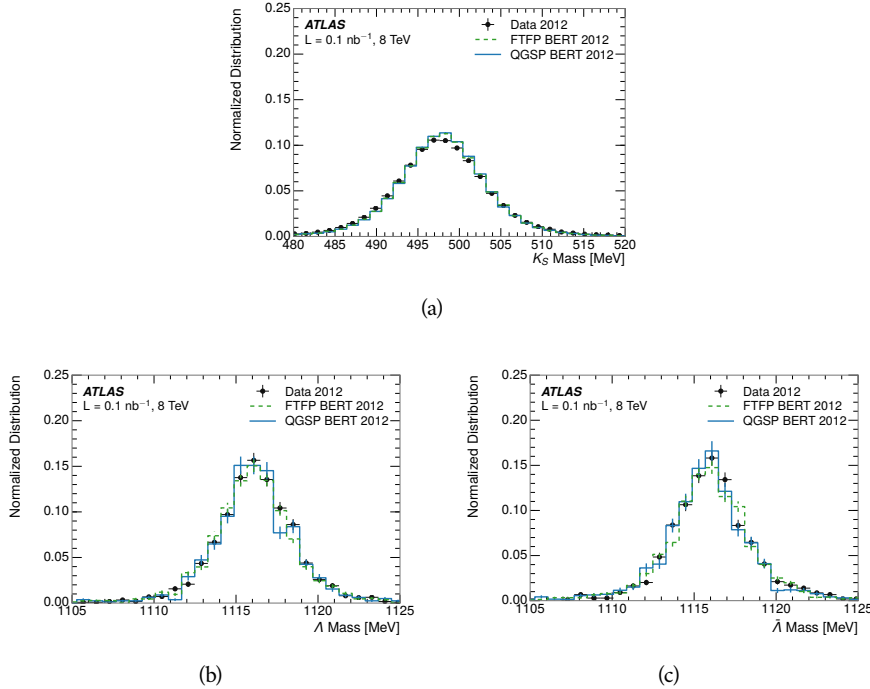


Figure 13: The reconstructed mass peaks of (a) K_S^0 , (b) Λ , and (c) $\bar{\Lambda}$ candidates.

The dominant backgrounds for the identified particle decays are nuclear interactions and combinatoric sources. These are suppressed by the kinematic requirements on the tracks as well as an additional veto which removes candidates that are consistent with both a Λ or $\bar{\Lambda}$ and a K_S^0 hypothesis, which is possible because of the different assumptions on particle mass in each case [5]. After these requirements, the backgrounds are found to be negligible compared to the statistical errors on these measurements.

8.3.2 IDENTIFIED RESPONSE

With these techniques the E/p distributions are extracted in data and simulation for each particle species and shown in Figure 14. These distributions are shown for a particular bin of E_a ($2.2 < E_a/\text{GeV} < 2.8$), rather than p . E_a is the energy available to be deposited in the calorimeter: for pions $E_a = \sqrt{p^2 + m^2}$, for protons $E_a = \sqrt{p^2 + m^2} - m$, and for antiprotons $E_a = \sqrt{p^2 + m^2} + m$. The features of the E/p distributions are similar to the inclusive case. There is a small negative tail from noise and a large fraction of tracks with zero energy from particles which do not reach the calorimeter. The long positive tail is noticeably more

678 pronounced for antiprotons because of the additional energy generated by the
 679 annihilation in addition to the neutral background.

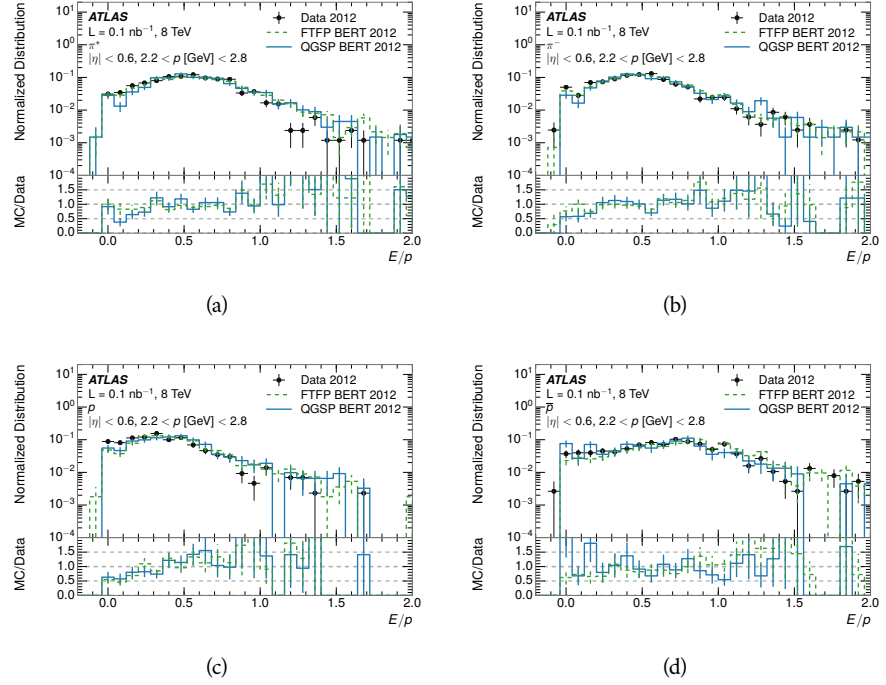


Figure 14: The E/p distribution for isolated (a) π^+ , (b) π^- , (c) proton, and (d) anti-proton tracks.

680 The zero fraction is further explored in Figure 15 for pions and protons in data
 681 and simulation. The simulation consistently underestimates the zero fraction
 682 independent of particle species, which implies that this discrepancy is not caused
 683 by the model of a particular species but rather a feature common to all.

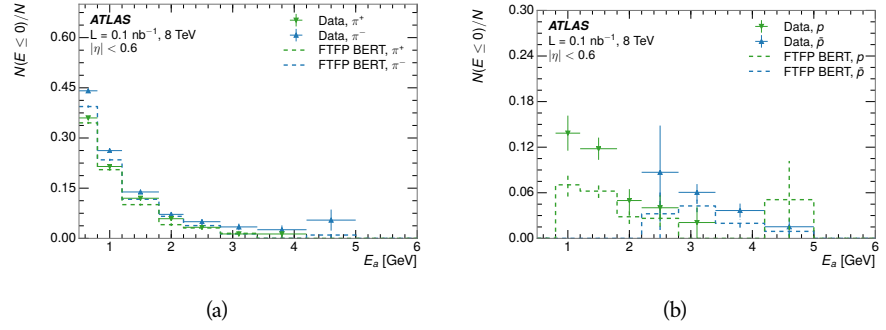


Figure 15: The fraction of tracks with $E \leq 0$ for identified (a) π^+ and π^- , and (b) proton and anti-proton tracks

684 It is also interesting to compare the response between the different particle
 685 species. One approach to do this is to measure the difference in $\langle E/p \rangle$ between
 686 two types, which has the advantage of removing the neutral background. These
 687 differences are shown in various combinations in Figure 16. The response for

π^+ is greater on average than the response to π^- because of a charge-exchange effect which causes the production of additional neutral pions in the showers of π^+ [27]. The response for π^+ is also greater on average than the response to p , because a large fraction of the energy of π^+ hadrons is converted to an electromagnetic shower [28, 29]. However, the \bar{p} response is significantly higher than the response to π^- because of the annihilation of the antiproton. FTFP_BERT does a better job of modeling this effect than QGSP_BERT because of their different descriptions of \bar{p} interactions with material.

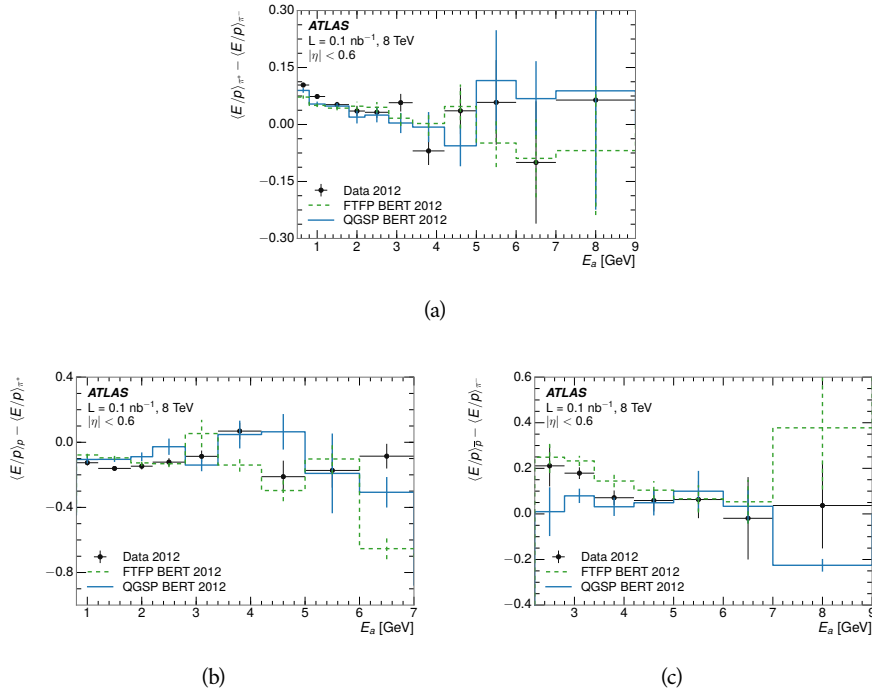


Figure 16: The difference in $\langle E/p \rangle$ between (a) π^+ and π^- (b) p and π^+ , and (c) \bar{p} and π^- .

It is also possible to remove the neutral background from these response distributions using the same technique as in Section 8.2.3. The technique is largely independent of the particle species and so can be directly applied to $\langle E/p \rangle$ for pions. The $\langle E/p \rangle_{\text{COR}}$ distributions for pions are shown in Figure 17, which are very similar to the inclusive results. The inclusive hadrons are comprised mostly of pions, so this similarity is not surprising. It is also possible to see the small differences between π^+ and π^- response here, where $\langle E/p \rangle_{\text{COR}}$ is higher on average for π^+ . The agreement between data and simulation is significantly worse for the π^- distributions than for the π^+ , with a discrepancy greater than 10% below 2-3 GeV.

8.3.3 ADDITIONAL SPECIES IN SIMULATION

The techniques above provide a method to measure the response separately for only pions and protons. However the hadrons which forms jets include a number of additional species such as kaons and neutrons. The charged kaons are

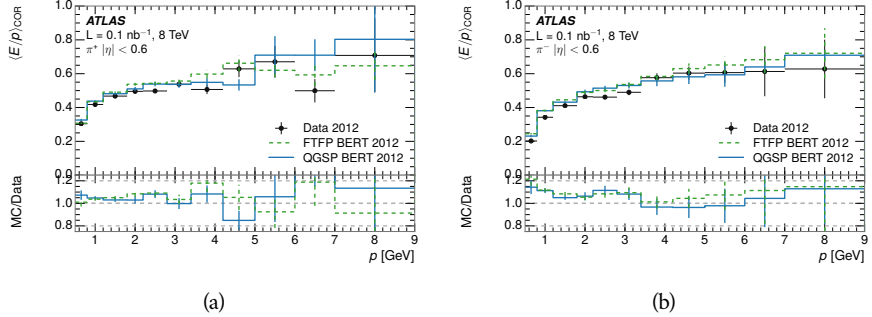


Figure 17: $\langle E/p \rangle_{\text{COR}}$ as a function of track momentum for (a) π^+ tracks and (b) π^- tracks.

an important component of the inclusive charged hadron distribution, which is comprised of roughly 60-70% pions, 15-20% kaons, and 5-15% protons. These are difficult to measure in data at the ATLAS detector, although a template subtraction technique has been proposed which may be effective with larger sample sizes [4]. The simulation of these particles includes noticeable differences in response at low energies, which are shown in Figure 18 for FTFP_BERT. The significant differences in response between low energy protons and antiprotons are accounted for above in the definitions of E_a .

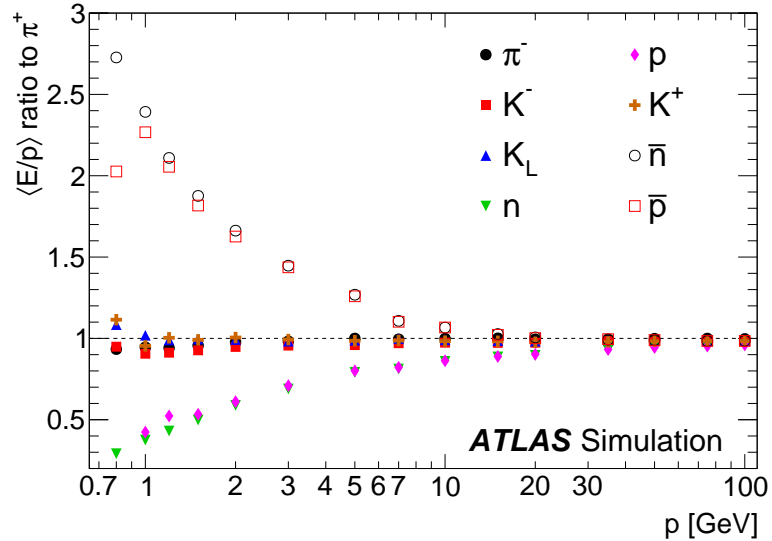


Figure 18: The ratio of the calorimeter response to single particles of various species to the calorimeter response to π^+ with the physics list FTFP_BERT.

718 8.4 SUMMARY

These various measurements of calorimeter response shown above for data and simulation illuminate the accuracy of the simulation of hadronic interactions at the ATLAS detector. The results were done using 2010 and 2012 data at 7 and 8

722 TeV, but reflect the most current understanding of the detector alignment and
723 geometry. A number of measurements focusing on a comparison between pro-
724 tons and antiprotons suggest that FTFP_BERT models those interaction more
725 accurately than QGSP_BERT. These measurements, among others, were the moti-
726 vation to switch the default Geant4 simulation from FTFP_BERT to QGSP_BERT
727 for all ATLAS samples.

728 Even with these updates, there are a number of small, approximately 5%, dis-
729 crepancies in response between the data and simulation at low energies. At
730 higher energies the simulation of hadronic interactions is very consistent with
731 data. Chapter 9 discusses how to use these observed differences to constrain the
732 jet energy scale and its associated uncertainties.

733

734 JET ENERGY RESPONSE AND UNCERTAINTY

735 9.1 MOTIVATION

736 As jets form a major component of many physics analyses at ATLAS, it is cru-
 737 cial to carefully calibrate the measurement of jet energies and to derive an un-
 738 certainty on that measurement. These uncertainties have often been the dom-
 739 inant systematic uncertainty in high-energy analyses at the Large Hadron Col-
 740 linder ([LHC](#)). Dijet and multijet balance techniques provide a method to constrain
 741 the [JES](#) and its uncertainty in data, and provide the default values used for ATLAS
 742 jet measurements at most energies [30]. These techniques are limited by their re-
 743 liance on measuring jets in data, so they are statistically limited in estimating
 744 the jet energy scale at the highest jet energies. This chapter presents another
 745 method for estimating the jet energy scale and its uncertainty which builds up a
 746 jet from its components and thus can be naturally extended to high jet momen-
 747 tum. Throughout this chapter the jets studied are simulated using [Pythia8](#) with
 748 the CT10 parton distribution set [31] and the AU2 tune [8], and corrections are
 749 taken from the studies including data and simulation in Chapter 8.

750 As described in Section 7.2, jets are formed from topological clusters of energy
 751 in the calorimeters using the anti- k_t algorithm. These clusters originate from a
 752 diverse spectrum of particles, in terms of both species and momentum, leading to
 753 significantly varied jet properties and response between jets of similar produced
 754 momentum. Figure 19 shows the simulated distribution of particles within jets
 755 at a few examples energies. The E/p measurements provide a thorough under-
 756 standing of the dominant particle content of jets, the charged hadrons.

757 9.2 UNCERTAINTY ESTIMATE

758 Simulated jets are not necessarily expected to correctly model the energy de-
 759 posits in the calorimeters, because of the various discrepancies discussed in Chap-
 760 ter 8. To evaluate a jet energy response, the simulated jet energies are compared
 761 to a corrected jet built up at the particle level. Each cluster in a jet is associated
 762 to the truth particle which deposited it, and the energy in that cluster is then
 763 corrected for a number of effects based on measurements in data. The primary
 764 corrections come from the single hadron response measurements in addition
 765 to response measured using the combined test beam which covers higher mo-
 766 mentum particles [32]. These corrections include both a shift (Δ), in order to
 767 make the simulation match the average response in data, and an uncertainty (σ)
 768 associated with the ability to constrain the difference between data and simula-
 769 tion. Some of the dominant sources of uncertainty are itemized in Table 1 with
 770 typical values, and the full list considered is described in detail in the associated

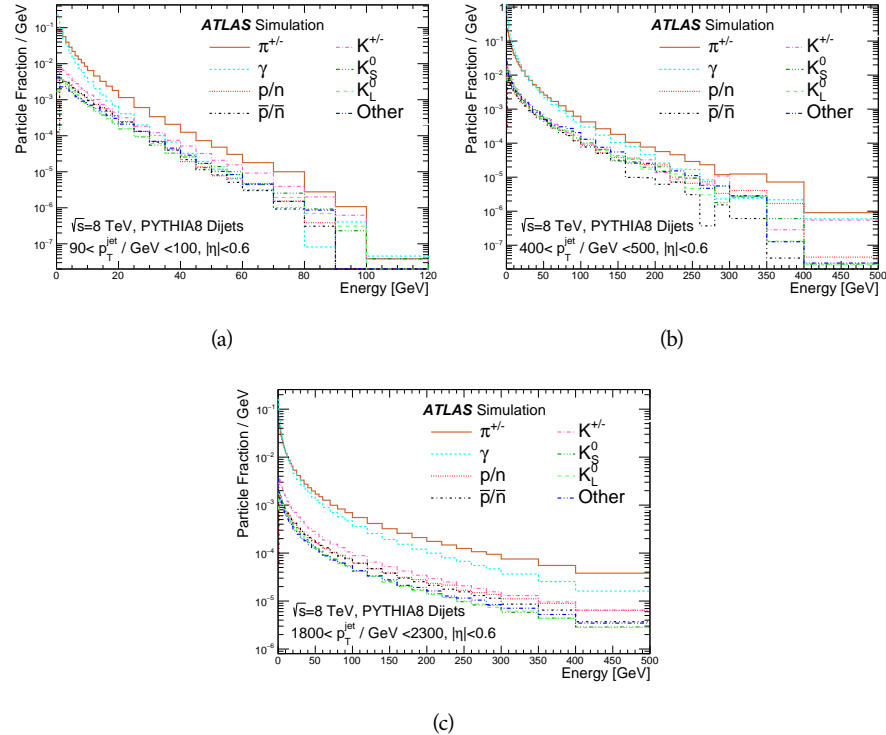


Figure 19: The spectra of true particles inside anti- k_t , $R = 0.4$ jets with (a) $90 < p_T/\text{GeV} < 100$, (b) $400 < p_T/\text{GeV} < 500$, and (c) $1800 < p_T/\text{GeV} < 2300$.

paper [4]. These uncertainties cover differences between the data and simulation in the modeling of calorimeter response to a given particle. No uncertainties are added for the difference between particle composition of jets in data and simulation.

From these terms, the jet energy scale and uncertainty is built up from individual energy deposits in simulation. Each uncertainty term is treated independently, and are taken to be gaussian distributed. The resulting scale and uncertainty is shown in Figure 20, where the mean response is measured relative to the calibrated energy reported by simulation. The dominant uncertainties come from the statistical uncertainties on the E/p measurements at lower energies and the additional uncertainty for out of range measurements at higher energies. The total uncertainty from this method at intermediate jet energies is comparable to other simulation-based methods [33] and is about twice as large as in-situ methods using data [30]. This method is the only one which provides an estimation above 1.8 TeV, however, and so is still a crucial technique in analyses that search for very energetic jets.

These techniques can also be used to measure the correlation between bins of average reconstructed jet momentum across a range of p_T and $|\eta|$, where correlations are expected because of a similarity in particle composition at similar energies. Figure 21 shows these correlations, where the uncertainties on jets in neighboring bins are typically between 30% and 60% correlated. The uncertainty on all jets becomes significantly correlated at high energies and larger pseudora-

Abbrev.	Description	Δ (%)	σ (%)
In situ E/p	The comparison of $\langle E/p \rangle_{\text{COR}}$ as described in Chapter 8 with statistical uncertainties from 500 MeV to 20 GeV.	0-3	1-5
CTB	The main $\langle E/p \rangle$ comparison uncertainties, binned in p and $ \eta $, as derived from the combined test beam results, from 20 to 350 GeV [32].	0-3	1-5
E/p Zero Fraction	The difference in the zero-fraction between data and MC simulation from 500 MeV to 20 GeV.	5-25	1-5
E/p Threshold	The uncertainty in the EM calorimeter response from the potential mismodeling of threshold effects in topological clustering.	0	0-10
Neutral	The uncertainty in the calorimeter response to neutral hadrons based on studies of physics model variations.	0	5-10
K_L	An additional uncertainty in the response to neutral K_L in the calorimeter based on studies of physics model variations.	0	20
E/p Misalignment	The uncertainty in the p measurement from misalignment of the ID.	0	1
Hadrons, $p > 350$ GeV	A flat uncertainty for all particles above the energy range or outside the longitudinal range probed with the combined test beam.	0	10

Table 1: The dominant sources of corrections and systematic uncertainties in the [JES](#) estimation technique, including typical values for the correcting shift (Δ) and the associated uncertainty (σ).

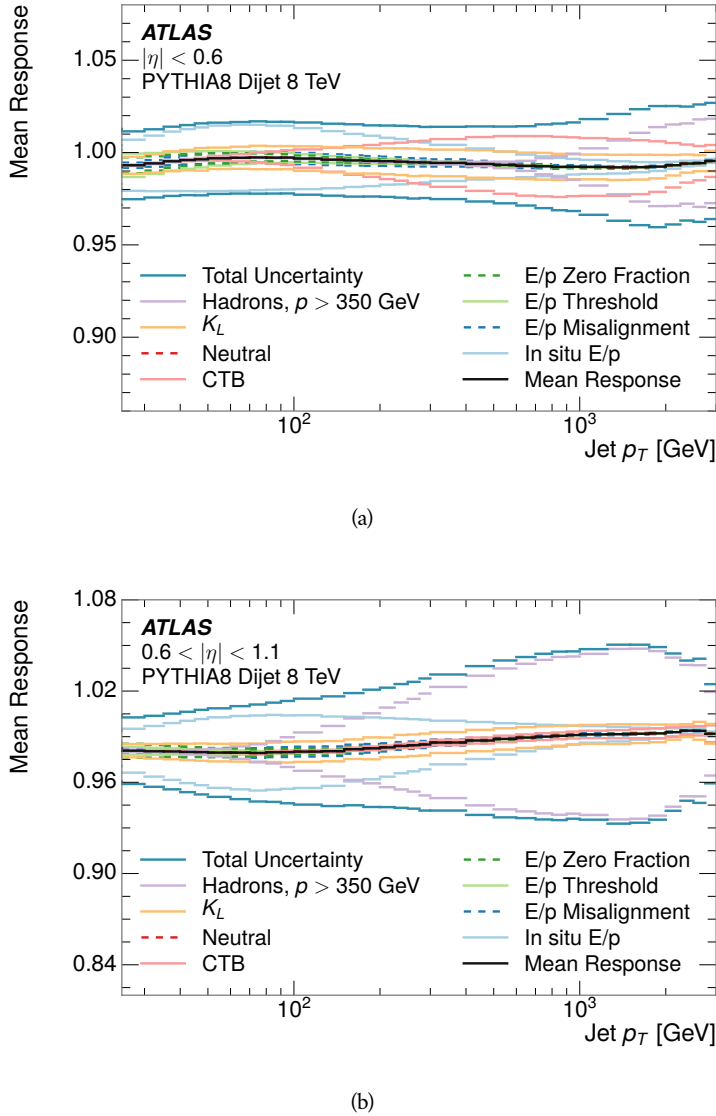


Figure 20: The [JES](#) uncertainty contributions, as well as the total [JES](#) uncertainty, as a function of jet p_T for (a) $|\eta| < 0.6$ and (b) $0.6 < |\eta| < 1.1$.

793 pidities, when the uncertainty becomes dominated by the single term reflecting
 794 out of range particles.

795 9.3 SUMMARY

796 The technique described above provides a jet energy scale and uncertainty by
 797 building up jet corrections from the energy deposits of constituent particles. The
 798 E/p measurements are crucial in providing corrections for the majority of parti-
 799 cles in the jets. The uncertainty derived this way is between 2 and 5% and is about
 800 twice as large at corresponding momentum than jet balance methods. However
 801 this is the only uncertainty available for very energetic jets using 2012 data and
 802 simulation, and repeating this method with Run 2 data and simulation will be

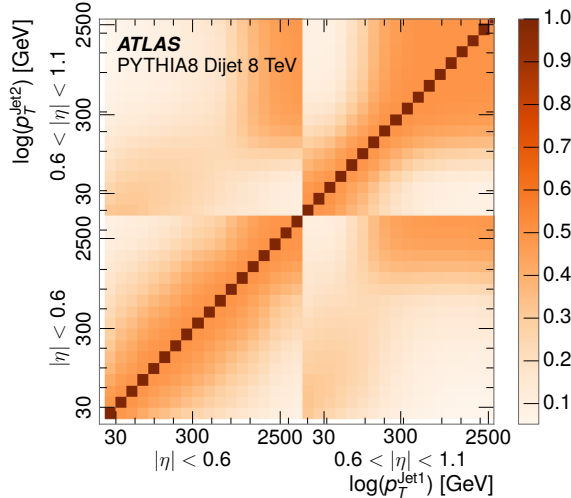


Figure 21: The JES correlations as a function of jet p_T and $|\eta|$ for jets in the central region of the detector.

803 important in providing an uncertainty for the most energetic jets in 13 TeV col-
 804 lisions.

805

PART V

806

SEARCH FOR LONG-LIVED PARTICLES

807

You can put some informational part preamble text here.

10

808

809 LONG-LIVED PARTICLES IN ATLAS

810 10.1 OVERVIEW AND CHARACTERISTICS

811 10.2 SIMULATION

812

813 EVENT SELECTION

814 The Long-Lived Particles ([LLPs](#)) targeted by this search differ in their interactions
 815 with the detector from [SM](#) particles primarily because of their large mass. When
 816 produced at the energies available at the [LHC](#), that large mass results in a low β
 817 and such slow-moving particles heavily ionize in detector material. Each layer
 818 of the pixel detector provides a measurement of that ionization, through time
 819 over threshold ([ToT](#)), as discussed in Section [6.3.1](#). The ionization in the pixel
 820 detector, quantified in terms of dE/dx , provides the major focus for this search
 821 technique, both for its discriminating power and also because of the large range
 822 of lifetimes where it can be used. The dE/dx variable needs to be augmented
 823 with a few additional selection requirements to form a complete search.

824 Ionization is not currently available in any form during triggering, so this
 825 search instead relies on E_T^{miss} to trigger signal events. Although triggering on
 826 E_T^{miss} is not particularly efficient, E_T^{miss} is often large for many production mech-
 827 anisms of [LLPs](#), as discussed in Section [10.1](#).

828 Ionization is most effective in rejecting backgrounds for well-measured, high-
 829 momentum tracks, so some basic requirements on quality and kinematics are
 830 placed on the particles considered in this search. In particular a newly intro-
 831 duced tracking variable is very effective in removing highly-ionizing backgrounds
 832 caused by overlapping tracks. A few additional requirements are placed on the
 833 tracks considered for [LLP](#) candidates that increase background rejection by tar-
 834 geting specific types of [SM](#) particles. These techniques provide a significant anal-
 835 ysis improvement over previous iterations of ionization-based searches on AT-
 836 LAS by providing additional background rejection with minimal loss in signal
 837 efficiency.

838 The ionization measurement with the Pixel detector can be calibrated to pro-
 839 vide an estimator of $\beta\gamma$. That estimate, together with the momentum measure-
 840 ment provided by tracking, can be used to reconstruct a mass for each track
 841 which traverses the pixel detector. That mass variable will be peaked at the [LLP](#)
 842 mass for any signal, and provides an additional tool to search for an excess. In
 843 addition to an explicit requirement on ionization, this search constructs a mass-
 844 window for each targeted mass range in order to evaluate any excess of events
 845 and to set limits.

846 The strategy discussed here is optimized for lifetimes of $O(1) - O(10)$ ns.
 847 Pixel ionization is especially useful in this regime as particles only need to prop-
 848 agate through the first seven layers of the inner detector, about 37 cm from the
 849 beam axis. The search is still competitive with other searches for [LLPs](#) at longer
 850 lifetimes, because the primary discriminating variables are still applicable even
 851 for particles that do not decay within the detector [34]. Although the basic strat-
 852 egy remains the same for all lifetimes, two signal regions are defined to optimize
 853 separately for intermediate and long lifetime particles.

854 11.1 TRIGGER

855 Triggering remains a significant difficulty in defining an event selection with
 856 high signal efficiency in a search for [LLPs](#). There are no triggers available in
 857 the current ATLAS system that can fire directly from a high momentum track
 858 with large ionization (Section 6.6). Although in some configurations a charged
 859 [LLP](#) can fire muon triggers, this requirement introduces significant model depen-
 860 dence on both the allowed lifetimes and the interactions in the calorimeter [35].

861 For a search targetting particles which may decay prior to reaching the muon
 862 system, the most efficient available trigger is based on missing energy [35]. As
 863 discussed in Section 10.1, signal events can produce E_T^{miss} by two primary mech-
 864 anisms. The decays of R-Hadrons to neutralinos can produce missing energy
 865 when the neutralinos go undetected in the calorimeters. [LLPs](#) which do not de-
 866 cay before the calorimeters also can produce missing energy because they do not
 867 deposit much energy. Either case to some extent relies on kinematic degrees of
 868 freedom to produce missing energy, as the pair-produced [LLPs](#) tend to balance
 869 each other in the transverse plain. That balance results in a relatively low ef-
 870 ficiency for long-lifetime particles, roughly 40%, and efficiencies between 65%
 871 and 95% for shorter lifetimes depending on both the mass and the lifetime.

872 11.2 KINEMATICS AND ISOLATION

873 After the trigger requirement, each event is required to have a primary vertex
 874 reconstructed from at least two well-measured tracks in the inner detector, each
 875 with $p_T > 400$ MeV. If more than one such vertex exists, the primary vertex is
 876 taken to be the one with the largest summed track momentum for all tracks as-
 877 sociated to that vertex. The offline reconstructed E_T^{miss} is required to be above
 878 130 GeV to additionally reject [SM](#) backgrounds. The transverse missing energy
 879 is calculated using fully reconstructed and calibrated offline objects, as described
 880 in Section 7.5. In particular the E_T^{miss} definition in this selection uses jets recon-
 881 structed with the anti- k_t algorithm with radius $R = 0.4$ from clusters of energy
 882 in the calorimeter (Section 7.2) and with $p_T > 20$ GeV, as well as reconstructed
 883 muons, electrons, and tracks not identified as another object type.

884 The E_T^{miss} distributions are shown for data and a few simulated signals in Fig-
 885 ure 22, after the trigger requirement. The cut placed at 130 GeV is 95% effi-
 886 cient for metastable and 90% efficient for stable particles, because of the missing
 887 energy generating mechanisms discussed previously. The distribution of data
 888 in this figure and subsequent figures in this section can be interpreted as the
 889 distribution of backgrounds, as any signal contamination would be negligible if
 890 present at these early stages of the selection (prior to the final requirement on
 891 mass). The background falls rapidly with missing energy, motivating the direct
 892 requirement on E_T^{miss} for the signal region. Although a tigher requirement than
 893 the specified value of 130 GeV would seem to increase the search potential from
 894 these early distributions, other requirements are more optimal when taken as a
 895 whole. The specific values for each requirement in signal region were optimized
 896 considering the increase in discovery reach for tightening the requirement on

897 each discriminating variable. **NOTE: Is it interesting to discuss the signal re-**
 898 **gion optimization process in detail? I could add another section on how**
 899 **the values were determined, although in truth it is at least partially histor-**
 900 **ical precedence.**

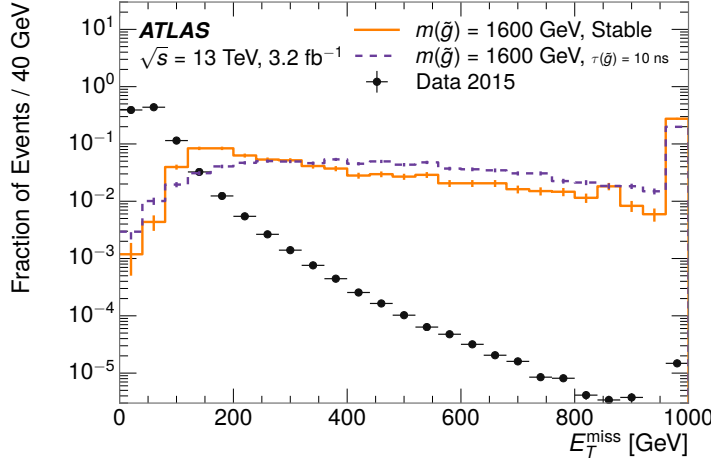


Figure 22: The distribution of E_T^{miss} for data and simulated signal events, after the trigger requirement.

901 Potential signal events are then required to have at least one candidate [LLP](#)
 902 track. Although the [LLPs](#) are produced in pairs, many models do not consistently
 903 yield two charged particles. For example, in the R-Hadron model highlighted
 904 here, only 20% of events have two charged R-Hadrons while 47% of events have
 905 just one. A signal region requiring two charged candidates could be a powerful
 906 improvement in background rejection for a larger dataset, but it is not consid-
 907 ered in this version of the analysis as it was found to be unnecessary to reject the
 908 majority of backgrounds.

909 For a track to be selected as a candidate, it must have $p_T > 50 \text{ GeV}$ and pass
 910 basic quality requirements. The track must be associated to the primary vertex.
 911 It must also have at least seven clusters in the silicon layers in the inner detector
 912 to ensure an accurate measurement of momentum. Those clusters must include
 913 one in the innermost layer if the extrapolated track is expected to pass through
 914 that layer. And to ensure a reliable measurement of ionization, the track is re-
 915 quired to have at least two clusters in the pixel detector that provide a measure-
 916 ment of dE/dx .

917 At this point in the selection, there is a significant high-ionization background
 918 from multiple tracks that significantly overlap in the inner detector. Previous
 919 version of this analysis have rejected these overlaps by an explicit overlap rejec-
 920 tion between pairs of fully reconstructed tracks, typically by requiring no addi-
 921 tional tracks within a cone around the candidate. This technique, however, fails
 922 to remove the background from tracks that overlap so precisely that the tracks
 923 cannot be separately resolved.

924 A new method, added in Run 2, identifies cluster shapes that are likely formed
 925 by multiple tracks based on a neural network classification algorithm. The num-

926 ber of clusters that are classified this way in the pixel detector for a given track
 927 is called N_{split} . As the shape of clusters requires significantly less spatial sepa-
 928 ration to identify overlaps than it does to reconstruct two fully resolved tracks,
 929 this variable is more effective at rejecting backgrounds from overlaps. Figure 23
 930 shows the dependence of ionization on N_{split} ; as N_{split} increases the mean of
 931 dE/dx grows significantly up to twice the expected value when $N_{\text{split}} = 4$.

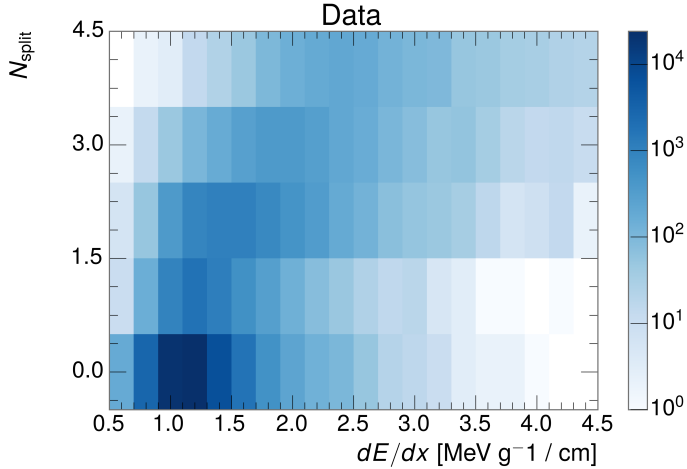


Figure 23: The dependence of dE/dx on N_{split} in data after basic track hit requirements have been applied.

932 This requirement is very successful in reducing the long positive tail of the
 933 dE/dx distributions, as can be seen in Figure 24. Comparing the distribution for
 934 “baseline tracks”, tracks with only the above requirements on clusters applied and
 935 before the requirement on N_{split} , to the distribution with $N_{\text{split}} = 0$, it is clear
 936 that the fraction of tracks with large dE/dx is reduced by several orders of mag-
 937 nitude. The isolated tracks are very close to the dE/dx distribution of identified
 938 muons, which are extremely well isolated on average. Figure 24 also includes
 939 the distribution of dE/dx in an example signal simulation to demonstrate how
 940 effective dE/dx is as a discriminating variable with this isolation applied. The
 941 background falls rapidly for $dE/dx > 1.8 \text{ MeVg}^{-1}\text{cm}^2$ while the majority of
 942 the signal, approximately 90% depending on the mass, falls above that threshold.
 943 Over 90% of LLP tracks in simulated signal events pass the N_{split} -based isolation
 944 requirement.

945 A few additional kinematic requirements are imposed to help reduce SM back-
 946 grounds. The momentum of the candidate track must be at least 150 GeV, and
 947 the uncertainty on that measurement must be less than 50%. The distribution of
 948 momentum is shown in Figure 25 for tracks in data and simulated signal events
 949 after the previously discussed requirements on clusters, transverse momentum,
 950 and isolation have been imposed. The signal particles are much harder on aver-
 951 age than their backgrounds because of the high energy interactions required to
 952 produce them. The transverse mass, m_T , defined as

$$m_T = \sqrt{2 p_T E_T^{\text{miss}} (1 - \cos(\Delta\phi(E_T^{\text{miss}}, \text{track})))} \quad (1)$$

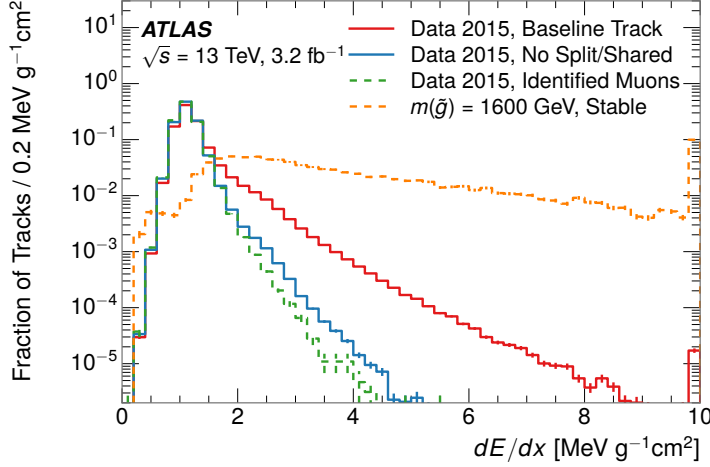


Figure 24: The distribution of dE/dx with various selections applied in data and simulated events.

estimates the mass of a decay of to a single charged particle and an undetected particle and is required to be greater than 130 GeV to reject contributions from the decay of W bosons. Figure 26 shows the distribution of m_T for data and simulated signal events. The signal is distributed over a wide range of m_T , with about 90% above the threshold value of 130 GeV. The data shows a dual-peaked structure, where the first peak comes from W boson decays and the second peak is a kinematic shaping from the requirements on E_T^{miss} and the track p_T in dijet events.

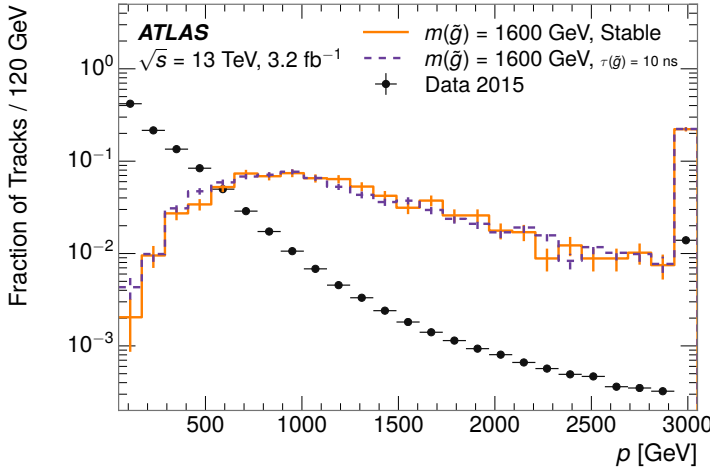


Figure 25: The distribution of track momentum for data and simulated signal events, after previous selection requirements have been applied.

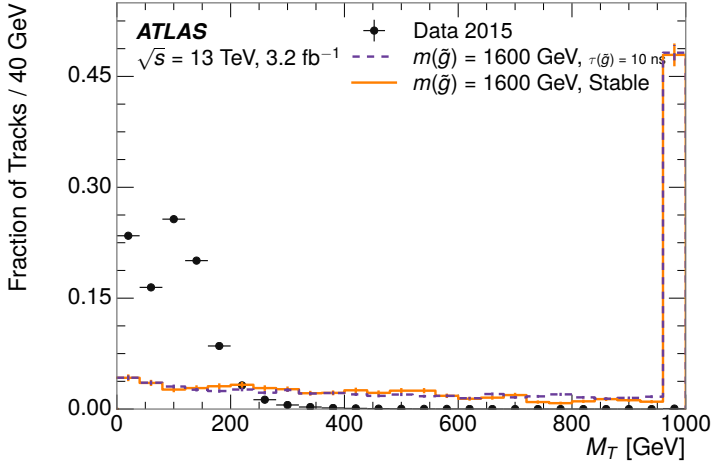


Figure 26: The distribution of M_T for data and simulated signal events, after previous selection requirements have been applied.

961 11.3 STANDARD MODEL REJECTION

962 Because the search selects events with just a single, highly-ionizing track, back-
 963 grounds can be formed by a wide variety of SM processes when various charged
 964 particles have a few randomly large deposits of energy in the pixel detector. Those
 965 backgrounds can be effectively rejected by targeting the types of particles pro-
 966 duced rather than the processes which produce them, as LLPs will have signifi-
 967 cant differences compared to any SM particle. These rejections focus on using
 968 additional features of the event, other than the kinematics or ionization of the
 969 candidate track, as it provides a powerful source of background rejection with
 970 very high signal efficiency. The lifetime of the particle can significantly change
 971 its detector characteristics, as discussed in Section 10.1. To accomodate these
 972 differences, the SM rejections defined in this section are split to form two signal
 973 regions, one for long-lifetimes particles, the “stable” region, and one for interme-
 974 diate lifetime particles, the “metastable” region.

975 Jets can be very effectively rejected by considering the larger-scale isolation of
 976 the candidate track. In this case the isolation focuses on the production of nearby
 977 particles as a jet-veto, rather than isolation from overlapping tracks to reduce
 978 high-ionization backgrounds. As explained in Section 10.1, the fragmentation
 979 process which produces an R-Hadron is very hard and thus is not expected to
 980 produce additional particles. The jet-veto uses the summed momentum of tracks
 981 with a cone of $\Delta R < 0.25$, referred to as p_T^{Cone} , which is shown in Figure 27 for
 982 data and simulated signal events. In the data this value has a peak at zero from
 983 isolated tracks such as leptons, and a long tail from jets which contains as much
 984 as 80% of the background above 20 GeV at this stage of the selection. In signal
 985 events p_T^{Cone} is strongly peaked at zero and significantly less than 1% is above 20
 986 GeV. This makes a requirement of $p_T^{\text{Cone}} < 20$ GeV one of the most effective
 987 methods to reject background without losing signal efficiency. For the stable

988 signal region, this cut is further tightened to $p_T^{\text{Cone}} < 5 \text{ GeV}$ as it is the most
 989 effective variable remaining to extend the search reach for long lifetimes.

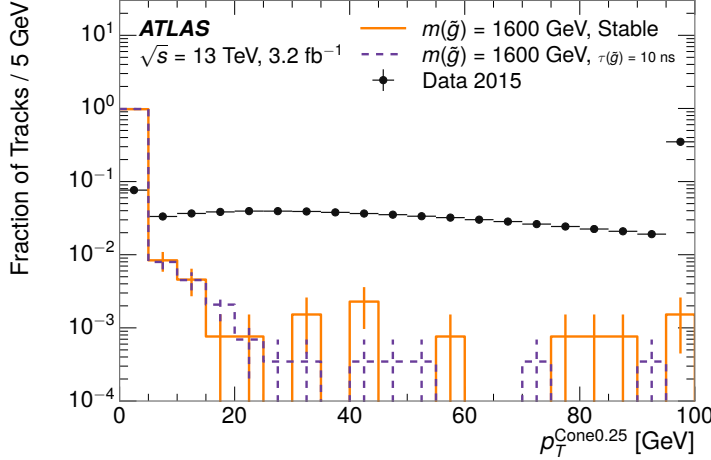


Figure 27: The distribution of summed tracked momentum within a cone of $\Delta R < 0.25$ around the candidate track for data and simulated signal events, after previous selection requirements have been applied.

990 Even for fully isolated particles, there are additional methods to reject each
 991 type of particle using information in the muon system and calorimeters. Muons
 992 can be identified very reliably using the tracks in the muon system, as described
 993 in Section 7.4. For intermediate lifetimes the LLPs do not survive long enough
 994 to reach the muon system, and so muons are vetoed by rejecting tracks that as-
 995 sociate to a muon with medium muon identification requirements. For longer
 996 lifetimes, this rejection is not applied because LLPs which reach the muon system
 997 can be identified as muons as often as 30% of the time in simulated samples.

998 Calorimeter-based particle rejection relies on the expected small deposits of
 999 energy from LLPs. When the lifetime is long enough to reach the calorimeter, a
 1000 LLP deposits little of its energy as it traverses the material, as discussed in Sec-
 1001 tion 10.1. Even when the particle does decay before the calorimeter, the major-
 1002 ity of its energy is carried away by the Lightest Supersymmetric Particle (LSP)
 1003 and not deposited in the calorimeter. In both cases the energy is expected to be
 1004 distributed across the layers of the calorimeters and not peaked in just one layer.
 1005 This can be quantified in terms of E/p , the ratio of calorimeter energy of a nearby
 1006 jet to the track momentum, and f_{EM} , the fraction of energy in that jet within the
 1007 electromagnetic calorimeter. When no jets fall within a cone of 0.05 of the par-
 1008 ticle, E/p and f_{EM} are both defined as zero. E/p is expected to be above 1.0
 1009 for typical SM particles because of calibration and the contributions from other
 1010 nearby particles. At these momenta there is no significant zero fraction due to
 1011 interactions with the detector or insufficient energy deposits (see Section 8.2.2).
 1012 f_{EM} is peaked close to 1.0 for electrons, and distributed between 10% and 90%
 1013 for hadrons.

1014 These trends can be seen in the two dimensional distribution for signal in Fig-
 1015 ure 28 for stable and metastable (10 ns) events. The majority of R-Hadrons in

1016 both samples fall into the bin for $E/p = 0$ and $f_{\text{EM}} = 0$ because the majority of
 1017 the time there is no associated jet. In the stable sample, when there is an associ-
 1018 ated jet, E/p is typically still below 0.1, and the f_{EM} is predominantly under 0.8.
 1019 In the metastable sample, on the other hand, E/p is larger but still typically below
 1020 0.1 because of actual jets produced during the decay. The f_{EM} is much lower on
 1021 average in this case, below 0.1, because the 10 ns lifetime particles rarely decay
 1022 before passing through the electromagnetic calorimeter. Figure 28 also includes
 1023 simulated Z decays to electrons or tau leptons. From the decays to electrons it is
 1024 clear that the majority of electrons have f_{EM} above 0.9. The tau decays include a
 1025 variety of products. Muons can be seen in the bin where $E/p = 0$ and $f_{\text{EM}} = 0$
 1026 because they do not have an associated jet. Electrons fall into the range where
 1027 $E/p > 1$ and $f_{\text{EM}} > 0.9$. Hadronic tau decays are the most common, and fall in
 1028 the range of $0.1 < f_{\text{EM}} < 0.9$ and $E/p > 1.0$.

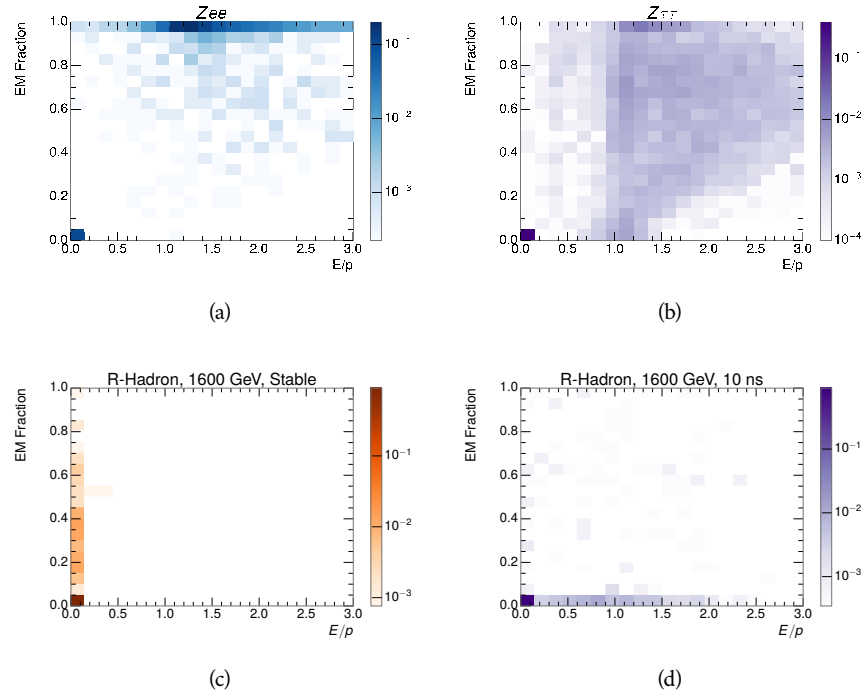


Figure 28: The normalized, two-dimensional distribution of E/p and f_{EM} for simulated
 (a) $Z \rightarrow ee$, (b) $Z \rightarrow \tau\bar{\tau}$, (c) 1200 GeV Stable R-Hadron events, and (d) 1200
 GeV, 10 ns R-Hadron events.

1029 These differences motivate an electron rejection by requiring an f_{EM} below
 1030 0.9. Similarly, isolated hadrons are rejected by requiring $E/p < 1.0$. These re-
 1031 quirements combine to remove the majority of isolated electrons and hadrons
 1032 but retain over 95% of the simulated signal across a range of masses and lifetimes.

1033 11.4 IONIZATION

1034 The final requirements on the candidate track are the primary discriminating
 1035 variables, the ionization in the pixel detector and the corresponding mass. That

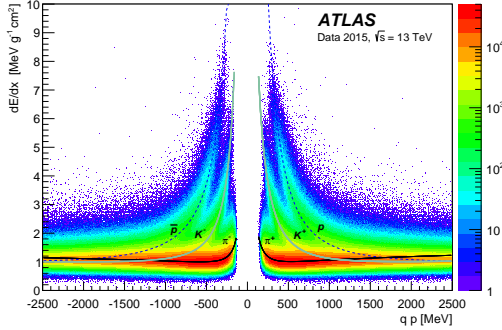


Figure 29: Two-dimensional distribution of dE/dx versus charge signed momentum (qp) for minimum-bias tracks. The fitted distributions of the most probable values for pions, kaons and protons are superimposed.

ionization is measured in terms of dE/dx , which was shown for data and simulated signal events in Figure 24. dE/dx is dramatically greater for the high mass signal particles than the backgrounds, which start to fall immediately after the minimally ionizing peak at $1.1 \text{ MeVg}^{-1}\text{cm}^2$. The dE/dx for candidate tracks must be greater than a pseudorapidity-dependent threshold, specifically $1.80 - 0.11|\eta| + 0.17\eta^2 - 0.05|\eta|^3 \text{ MeV g}^{-1} \text{ cm}^{-2}$, in order to correct for an approximately 5% dependence of the MIP peak on η . The requirement was chosen as part of the signal region optimization, and manages to reduce the backgrounds by a factor of 100 while remaining 70-90% efficient for simulated signal events depending on the mass.

11.4.1 MASS ESTIMATION

The mean value of ionization in silicon is governed by the Bethe-Bloch formula and the most probable value follows a Landau-Vavilov distribution [36]. Those forms inspire a parametric description of dE/dx in terms of $\beta\gamma$,

$$(dE/dx)_{\text{MPV}}(\beta\gamma) = \frac{p_1}{\beta^{p_3}} \ln(1 + [p_2\beta\gamma]^{p_5}) - p_4 \quad (2)$$

which performs well in the range $0.3 < \beta\gamma < 1.5$. This range includes the expected range of $\beta\gamma$ for the particles targeted for this search, with $\beta\gamma \approx 2.0$ for lower mass particles ($O(100 \text{ GeV})$) and up to $\beta\gamma \approx 0.5$ for higher mass particles ($O(1000 \text{ GeV})$). The parameters, p_i , are fit using a 2015 data sample of low-momentum pions, kaons, and protons as described in Ref. [37]. Figure 29 shows the two-dimensional distribution of dE/dx and momentum along with the above fitted values for $(dE/dx)_{\text{MPV}}$.

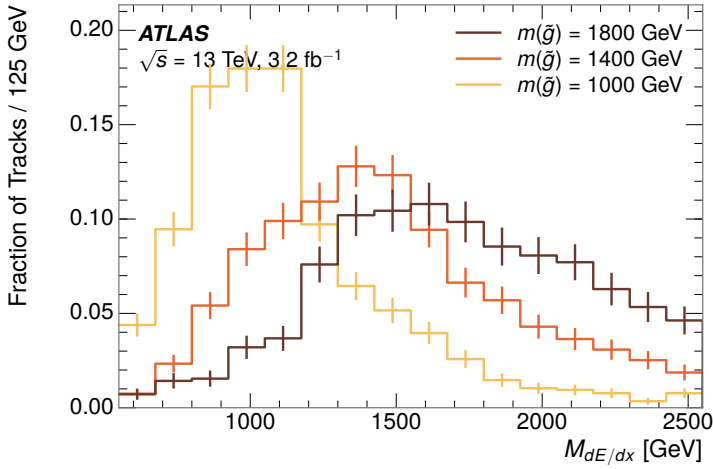


Figure 30: The distribution of mass estimated using dE/dx for simulated stable R-Hadrons with masses between 1000 and 1600 GeV.

The above equation (2) is then numerically inverted to estimate $\beta\gamma$ and then mass for each candidate track. In simulated signal events, the mean of this mass value reproduces the generated mass up to around 1800 GeV to within 3%, and 3% shift is applied to correct for this difference. The mass distributions prior to this correction are shown for a few stable mass points in Figure 30. The large widths of these distributions come from the high variability in energy deposits in the pixel detector, but the means converge to the expected values.

This analysis evaluates expected yields and the resulting cross sectional limits using windows in this mass variable. The windows are formed by fitting mass distributions like those in Figure 30 to Gaussian distribution and taking all events that fall within $\pm 1.4\sigma$ of the mean. As can be seen in Figure 30, typical values for this width are $\sigma \approx 300 - 500$ GeV depending on the generated mass.

11.5 EFFICIENCY

The numbers of events passing each requirement through ionization are shown in Table 2 for the full 2015 dataset and a simulated 1600 GeV, 10 ns lifetime R-Hadron sample. The table highlights the overall acceptance \times efficiency for signal events, which for this example is 19%. Between SM rejection and ionization, this signal region reduces the background of tracks which pass the kinematic requirements down by an additional factor of almost 2000.

There is a strong dependence of this efficiency on lifetime and mass, with efficiencies dropping to under 1% at low lifetimes. Figure 31 shows the dependence on both mass and lifetime for all signal samples considered in this search. The dependence on mass is relatively slight and comes predominantly from the increasing fraction of R-Hadrons which pass the ionization cut with increasing mass. The trigger and E_T^{miss} requirements are most efficient for particles that decay before reaching the calorimeters. However, the chance of a particle to be

Selection	Exp. Signal Events	Observed Events in 3.2 fb^{-1}
Generated	26.0 ± 0.3	
E_T^{miss} Trigger	24.8 ± 0.3 (95%)	
$E_T^{\text{miss}} > 130 \text{ GeV}$	23.9 ± 0.3 (92%)	
Track Quality and $p_T > 50$	10.7 ± 0.2 (41%)	368324
Isolation Requirement	9.0 ± 0.2 (35%)	108079
Track $p > 150 \text{ GeV}$	6.6 ± 0.2 (25%)	47463
$m_T > 130 \text{ GeV}$	5.8 ± 0.2 (22%)	18746
Electron and Hadron Veto	5.5 ± 0.2 (21%)	3612
Muon Veto	5.5 ± 0.2 (21%)	1668
Ionization Requirement	5.0 ± 0.1 (19%)	11

Table 2: The expected number of events at each level of the selection for metastable 1600 GeV , 10 ns R-Hadrons, along with the number of events observed in data, for 3.2 fb^{-1} . The simulated yields are shown with statistical uncertainties only. The total efficiency \times acceptance is also shown for the signal.

1083 reconstructed as a high-quality track decreases significantly at low lifetimes as
 1084 the particle does not propagate sufficiently through the inner detector. These
 1085 effects lead to a maximum in the selection efficiency for lifetimes around 10-30
 1086 ns.

1087 The inefficiency of this signal region at short lifetimes comes almost exclu-
 1088 sively from an acceptance effect, in that the particles do not reach the necessar-
 1089 ily layers of the SCT. This can be seen more clearly by defining a fiducial region
 1090 which includes events with at least one R-Hadron that is produced with non-
 1091 zero charge, $p_T > 50 \text{ GeV}$, $p > 150 \text{ GeV}$, $|\eta| < 2.5$, and a decay distance greater
 1092 than 37 cm in the transverse plane. At short (1 ns) lifetimes, the acceptance into
 1093 this region is as low as 4%. Once this acceptance is accounted for, the selection
 1094 efficiency ranges from 25% at lifetimes of 1 ns up to 45% at lifetimes of 10 ns.

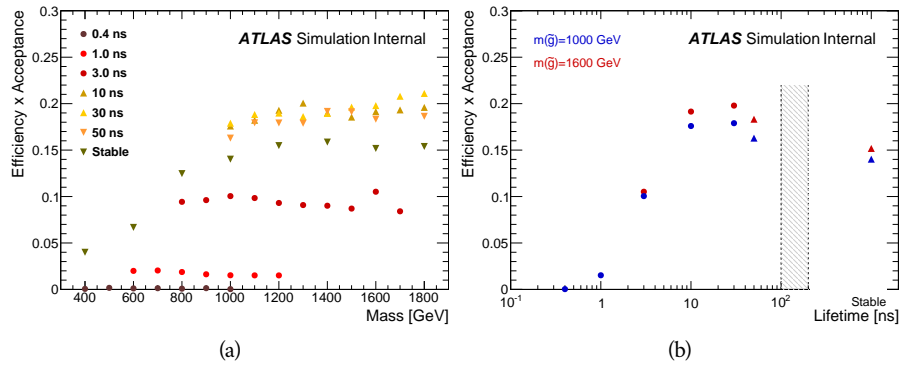


Figure 31: The acceptance \times efficiency as a function of R-Hadron (a) mass and (b) lifetime. (a) shows all of the combinations of mass and lifetime considered in this search, and (b) highlights the lifetime dependence for 1000 GeV and 1600 GeV R-Hadrons.

1095

1096 BACKGROUND ESTIMATION

1097 The event selection discussed in the previous section focuses on detector signa-
 1098 tures, emphasizing a single high-momentum, highly-ionizing track. That track
 1099 is then required to be in some way inconsistent with the expected properties
 1100 of SM particles, with various requirements designed to reject jets, hadrons,
 1101 electrons, and muons (Section 11.3). Were these selections perfectly effective, the sig-
 1102 nal region would be entirely empty in data. So the background from this search
 1103 comes entirely from reducible backgrounds that are outliers of various distribu-
 1104 tions like momentum, dE/dx , and p_T^{Cone} . The simulation can be tuned in various
 1105 ways to do an excellent job of modeling the average properties of each particle
 1106 type [38], but it is not necessarily expected to accurately reproduce outliers. For
 1107 these reasons, the background estimation used for this search is estimated en-
 1108 tirely using data.

1109 12.1 BACKGROUND SOURCES

1110 Charged particles with lifetimes long enough to form tracks in the inner detector
 1111 can be grouped into three major categories based on their detector interactions:
 1112 hadrons, electrons, and muons. Every particle that enters into the background
 1113 for this search belongs to one of these types. Relatively pure samples of each of
 1114 these types can be formed in data by inverting the various rejection techniques
 1115 in Section 11.3. Specifically, muons are selected requiring Medium muon iden-
 1116 tification, electrons requiring $E/p > 1.0$ and $f_{\text{EM}} > 0.95$, and hadrons requiring
 1117 $E/p > 1.0$ and $f_{\text{EM}} < 0.95$.

1118 Figure 32 shows the distributions of momentum and dE/dx for these cate-
 1119 gories in data, after requiring the event level selection as well as the track re-
 1120 quirements on p_T , hits, and N_{split} , as discussed in Section 11.2. Simulated signal
 1121 events are included for reference. These distribution are only illustrative of the
 1122 differences between types, as the rejection requirements could alter their shape,
 1123 especially for momentum which enters directly into E/p and can indirectly af-
 1124 fect muon identification. However they do show a clear difference in both distri-
 1125 butions. Momentum is expected to vary significantly because of the production
 1126 mechanisms for the different species. dE/dx is different between types because
 1127 of incomplete isolation; although the requirement on N_{split} helps to reduce the
 1128 effect it does not completely remove the effect of overlaps. Muons are better
 1129 isolated and thus have the smallest fraction of dE/dx above the threshold of 1.8
 1130 MeVg $^{-1}$ cm 2 ; hadrons and electrons have a larger fraction above this threshold.

1131 It is difficult to determine what fraction of each particle type enters into the fi-
 1132 nal signal region. The background method will not have significant dependence
 1133 on the relative contributions of each species, but it is useful to understand the
 1134 differences between each when considering the various tests of the method.

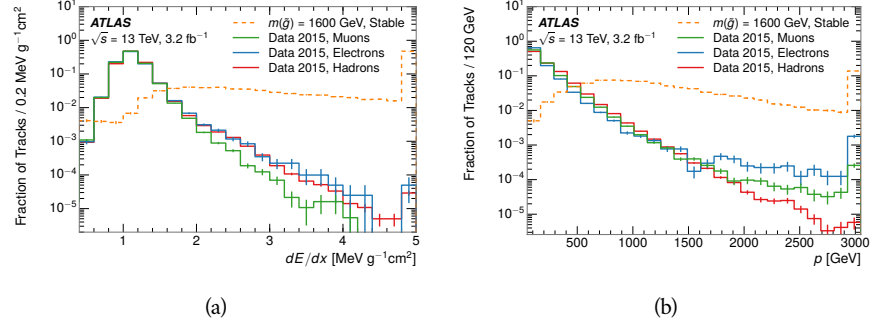


Figure 32: The distribution of (a) dE/dx and (b) momentum for tracks in data and simulated signal after requiring the event level selection and the track selection on p_T , hits, and N_{split} . Each subfigure shows the normalized distributions for tracks classified as hadrons, electrons, and muons in data and R-Hadrons in the simulated signal.

1135 12.2 PREDICTION METHOD

1136 The data-driven background estimation relies on the independence of ioniza-
 1137 tion and other aspects of the event. For standard model particles with momenta
 1138 above 50 GeV, dE/dx is not correlated with momentum. So, the proposed
 1139 method to estimate the mass distribution of the signal region is to use momen-
 1140 tumb from a track with low dE/dx (below the threshold value) and to combine it
 1141 with a random dE/dx value from a dE/dx template. The resulting track is just
 1142 as likely as the original, and so a number of such random generations forms a
 1143 distribution of mass for the signal region.

1144 Algorithmically this method is implemented by forming two distinct Control
 1145 Regions (**CRs**). The first **CR**, CR1, is formed by applying the entire event selection
 1146 from Chapter 11 up to the dE/dx and mass requirements. The dE/dx require-
 1147 ment is instead inverted for this region. Because of the independence of dE/dx ,
 1148 the tracks in this control region have the same kinematic distribution as the
 1149 tracks in the signal region, and are used to measure a two-dimensional template
 1150 of momentum and η . The second **CR**, CR2, is formed from the event selection
 1151 through the dE/dx requirement, but with an inverted E_T^{miss} requirement. The
 1152 tracks in this control region are expected to have similar dE/dx distributions
 1153 to the signal region, and so this region is used to measure a two-dimensional
 1154 template of dE/dx and η .

1155 The contribution of any signal to the control regions is minimized by the in-
 1156 verted selection requirements. Only less than 10% of simulated signal events
 1157 have either dE/dx or E_T^{miss} below the threshold values in the original signal re-
 1158 gion, while the backgrounds are significantly enhanced by inverting those re-
 1159 quirements. The signal contamination is less than 1% in both control regions
 1160 for all of the simulated masses and lifetimes considered in this analysis.

1161 With those measured templates, the shape of the mass estimation is generated
 1162 by first selecting a random p, η combination from CR1. This momentum value is
 1163 combined with a dE/dx value taken from the appropriate distribution of dE/dx

1164 for the selected η from CR2. The use of η in both random samplings controls for
1165 any correlation between p , dE/dx , and η . Those values are then used to calculate
1166 a mass in the same way that is done for regular tracks in data, see Section 11.4.1.
1167 As this procedure includes all dE/dx values, the cut at $1.8\text{MeVg}^{-1}\text{cm}^2$ is then
1168 enforced to fully model the signal region. The generated mass distribution is
1169 then normalized by scaling the background estimate to the data in the region
1170 $M < 160\text{ GeV}$, where signals of this type have already been excluded [39]. This
1171 normalization takes place before the ionization requirement.

1172 12.3 VALIDATION

1173 The validity of the background estimation can be evaluated in both data and sim-
1174 ulation. The underlying assumptions, that random combinations of dE/dx and
1175 momentum can predict a mass distribution in another region, can be tested us-
1176 ing simulated samples where concerns like multiple particle types can be con-
1177 trolled. Using the same technique in another set of signal-depleted regions in
1178 data then extends this confidence to the more complicated case where several
1179 particle species are inherently included.

1180 12.3.1 CLOSURE IN SIMULATION

1181 12.3.2 VALIDATION REGION IN DATA

13

1182

1183 SYSTEMATIC UNCERTAINTIES AND RESULTS

1184 13.1 SYSTEMATIC UNCERTAINTIES

1185 13.2 FINAL YIELDS

14

1186

1187 INTERPRETATION

1188 14.1 CROSS SECTIONAL LIMITS

1189 14.2 MASS LIMITS

1190 14.3 CONTEXT FOR LONG-LIVED SEARCHES

1191

PART VI

1192

CONCLUSIONS

1193

You can put some informational part preamble text here.

15

1194

1195 SUMMARY AND OUTLOOK

1196 15.1 SUMMARY

1197 15.2 OUTLOOK

1198

PART VII

1199

APPENDIX

1200

A

1201

1202 INELASTIC CROSS SECTION

B

1203

1204 APPENDIX TEST

1205 Examples: *Italics*, SMALL CAPS, ALL CAPS ¹. Acronym testing: **UML!** (**UML!**) –
1206 **UML! – UML! (UML!) – UML!s**

This appendix is temporary and is here to be used to check the style of the document.

1207 B.1 APPENDIX SECTION TEST

1208 Random text that should take up a few lines. The purpose is to see how sections
1209 and subsections flow with some actual context. Without some body copy be-
1210 tween each heading it can be difficult to tell if the weight of the fonts, styles, and
1211 sizes use work well together.

1212 B.1.1 APPENDIX SUBECTION TEST

1213 Random text that should take up a few lines. The purpose is to see how sections
1214 and subsections flow with some actual context. Without some body copy be-
1215 tween each heading it can be difficult to tell if the weight of the fonts, styles, and
1216 sizes use work well together.

1217 B.2 A TABLE AND LISTING

1218 Curabitur tellus magna, porttitor a, commodo a, commodo in, tortor. Donec in-
1219 terdum. Praesent scelerisque. Maecenas posuere sodales odio. Vivamus metus
1220 lacus, varius quis, imperdiet quis, rhoncus a, turpis. Etiam ligula arcu, elemen-
1221 tum a, venenatis quis, sollicitudin sed, metus. Donec nunc pede, tincidunt in,
1222 venenatis vitae, faucibus vel, nibh. Pellentesque wisi. Nullam malesuada. Morbi
1223 ut tellus ut pede tincidunt porta. Lorem ipsum dolor sit amet, consectetur adip-
1224 iscing elit. Etiam congue neque id dolor.

1225 There is also a Python listing below Listing 1.

1 Footnote example.

LABITUR BONORUM PRI NO	QUE VISTA	HUMAN
fastidii ea ius	germano	demonstratea
suscipit instructior	titulo	personas
quaestio philosophia	facto	demonstrated

Table 3: Autem usu id.

1226 B.3 SOME FORMULAS

Due to the statistical nature of ionisation energy loss, large fluctuations can occur in the amount of energy deposited by a particle traversing an absorber element². Continuous processes such as multiple scattering and energy loss play a relevant role in the longitudinal and lateral development of electromagnetic and hadronic showers, and in the case of sampling calorimeters the measured resolution can be significantly affected by such fluctuations in their active layers. The description of ionisation fluctuations is characterised by the significance parameter κ , which is proportional to the ratio of mean energy loss to the maximum allowed energy transfer in a single collision with an atomic electron:

You might get unexpected results using math in chapter or section heads. Consider the pdfspacing option.

$$\kappa = \frac{\xi}{E_{\max}} \quad (3)$$

E_{\max} is the maximum transferable energy in a single collision with an atomic electron.

$$E_{\max} = \frac{2m_e\beta^2\gamma^2}{1 + 2\gamma m_e/m_x + (m_e/m_x)^2},$$

1227 where $\gamma = E/m_x$, E is energy and m_x the mass of the incident particle, $\beta^2 =$
1228 $1 - 1/\gamma^2$ and m_e is the electron mass. ξ comes from the Rutherford scattering
1229 cross section and is defined as:

$$\xi = \frac{2\pi z^2 e^4 N_{Av} Z \rho \delta x}{m_e \beta^2 c^2 A} = 153.4 \frac{z^2}{\beta^2} \frac{Z}{A} \rho \delta x \text{ keV},$$

1230 where

z charge of the incident particle
 N_{Av} Avogadro's number
 Z atomic number of the material
 A atomic weight of the material
 ρ density
 δx thickness of the material
 1232 κ measures the contribution of the collisions with energy transfer close to
 1233 E_{\max} . For a given absorber, κ tends towards large values if δx is large and/or if
 1234 β is small. Likewise, κ tends towards zero if δx is small and/or if β approaches
 1235 1.

2 Examples taken from Walter Schmidt's great gallery:
<http://home.vrweb.de/~was/mathfonts.html>

Listing 1: A floating example (listings manual)

```
1 for i in xrange(10):
    print i, i*i, i*i*i
print "done"
```

1236 The value of κ distinguishes two regimes which occur in the description of
1237 ionisation fluctuations:

- 1238 1. A large number of collisions involving the loss of all or most of the incident
1239 particle energy during the traversal of an absorber.

1240 As the total energy transfer is composed of a multitude of small energy
1241 losses, we can apply the central limit theorem and describe the fluctua-
1242 tions by a Gaussian distribution. This case is applicable to non-relativistic
1243 particles and is described by the inequality $\kappa > 10$ (i. e., when the mean en-
1244 ergy loss in the absorber is greater than the maximum energy transfer in
1245 a single collision).

- 1246 2. Particles traversing thin counters and incident electrons under any condi-
1247 tions.

1248 The relevant inequalities and distributions are $0.01 < \kappa < 10$, Vavilov
1249 distribution, and $\kappa < 0.01$, Landau distribution.

1250 BIBLIOGRAPHY

- 1251 [1] S. Agostinelli et al. “GEANT4: A simulation toolkit”. In: *Nucl. Instrum. Meth.*
1252 A 506 (2003), pp. 250–303. doi: [10.1016/S0168-9002\(03\)01368-8](https://doi.org/10.1016/S0168-9002(03)01368-8).
- 1253 [2] ATLAS Collaboration. “A study of the material in the ATLAS inner de-
1254 tector using secondary hadronic interactions”. In: *JINST* 7 (2012), P01013.
1255 doi: [10.1088/1748-0221/7/01/P01013](https://doi.org/10.1088/1748-0221/7/01/P01013). arXiv: [1110.6191 \[hep-ex\]](https://arxiv.org/abs/1110.6191).
1256 [PERF-2011-08](#).
- 1257 [3] ATLAS Collaboration. “Electron and photon energy calibration with the
1258 ATLAS detector using LHC Run 1 data”. In: *Eur. Phys. J. C* 74 (2014), p. 3071.
1259 doi: [10.1140/epjc/s10052-014-3071-4](https://doi.org/10.1140/epjc/s10052-014-3071-4). arXiv: [1407.5063](https://arxiv.org/abs/1407.5063)
1260 [hep-ex]. [PERF-2013-05](#).
- 1261 [4] ATLAS Collaboration. “A measurement of the calorimeter response to sin-
1262 ggle hadrons and determination of the jet energy scale uncertainty using
1263 LHC Run-1 pp -collision data with the ATLAS detector”. In: (2016). arXiv:
1264 [1607.08842 \[hep-ex\]](https://arxiv.org/abs/1607.08842). [PERF-2015-05](#).
- 1265 [5] ATLAS Collaboration. “Single hadron response measurement and calorime-
1266 ter jet energy scale uncertainty with the ATLAS detector at the LHC”. In:
1267 *Eur. Phys. J. C* 73 (2013), p. 2305. doi: [10.1140/epjc/s10052-013-2305-1](https://doi.org/10.1140/epjc/s10052-013-2305-1). arXiv: [1203.1302 \[hep-ex\]](https://arxiv.org/abs/1203.1302). [PERF-2011-05](#).
- 1269 [6] ATLAS Collaboration. “The ATLAS Simulation Infrastructure”. In: *Eur.*
1270 *Phys. J. C* 70 (2010), p. 823. doi: [10.1140/epjc/s10052-010-1429-9](https://doi.org/10.1140/epjc/s10052-010-1429-9).
1271 arXiv: [1005.4568 \[hep-ex\]](https://arxiv.org/abs/1005.4568). [SOFT-2010-01](#).
- 1272 [7] T. Sjöstrand, S. Mrenna, and P. Skands. “A Brief Introduction to PYTHIA
1273 8.1”. In: *Comput. Phys. Commun.* 178 (2008), pp. 852–867. doi: [10.1016/j.cpc.2008.01.036](https://doi.org/10.1016/j.cpc.2008.01.036). arXiv: [0710.3820](https://arxiv.org/abs/0710.3820).
- 1275 [8] ATLAS Collaboration. *Summary of ATLAS Pythia 8 tunes*. ATL-PHYS-PUB-
1276 2012-003. 2012. URL: <http://cds.cern.ch/record/1474107>.
- 1277 [9] A.D. Martin, W.J. Stirling, R.S. Thorne, and G. Watt. “Parton distributions
1278 for the LHC”. In: *Eur. Phys. J. C* 63 (2009). Figures from the [MSTW Website](#),
1279 pp. 189–285. doi: [10.1140/epjc/s10052-009-1072-5](https://doi.org/10.1140/epjc/s10052-009-1072-5). arXiv: [0901.0002](https://arxiv.org/abs/0901.0002).
- 1281 [10] A. Sherstnev and R.S. Thorne. “Parton Distributions for LO Generators”.
1282 In: *Eur. Phys. J. C* 55 (2008), pp. 553–575. doi: [10.1140/epjc/s10052-008-0610-x](https://doi.org/10.1140/epjc/s10052-008-0610-x). arXiv: [0711.2473](https://arxiv.org/abs/0711.2473).
- 1284 [11] A. Ribon et al. *Status of Geant4 hadronic physics for the simulation of LHC*
1285 *experiments at the start of LHC physics program*. CERN-LCGAPP-2010-02.
1286 2010. URL: <http://lcgapp.cern.ch/project/docs/noteStatusHadronic2010.pdf>.

- 1288 [12] M. P. Guthrie, R. G. Alsmiller, and H. W. Bertini. "Calculation of the cap-
 1289 ture of negative pions in light elements and comparison with experiments
 1290 pertaining to cancer radiotherapy". In: *Nucl. Instrum. Meth.* 66 (1968), pp. 29–
 1291 36. doi: [10.1016/0029-554X\(68\)90054-2](https://doi.org/10.1016/0029-554X(68)90054-2).
- 1292 [13] H. W. Bertini and P. Guthrie. "News item results from medium-energy
 1293 intranuclear-cascade calculation". In: *Nucl. Instr. and Meth. A* 169 (1971),
 1294 p. 670. doi: [10.1016/0375-9474\(71\)90710-X](https://doi.org/10.1016/0375-9474(71)90710-X).
- 1295 [14] V.A. Karmanov. "Light Front Wave Function of Relativistic Composite
 1296 System in Explicitly Solvable Model". In: *Nucl. Phys. B* 166 (1980), p. 378.
 1297 doi: [10.1016/0550-3213\(80\)90204-7](https://doi.org/10.1016/0550-3213(80)90204-7).
- 1298 [15] H. S. Fesefeldt. *GHEISHA program*. Pitha-85-02, Aachen. 1985.
- 1299 [16] G. Folger and J.P. Wellisch. "String parton models in Geant4". In: (2003).
 1300 arXiv: [nucl-th/0306007](https://arxiv.org/abs/nucl-th/0306007).
- 1301 [17] N. S. Amelin et al. "Transverse flow and collectivity in ultrarelativistic
 1302 heavy-ion collisions". In: *Phys. Rev. Lett.* 67 (1991), p. 1523. doi: [10.1103/PhysRevLett.67.1523](https://doi.org/10.1103/PhysRevLett.67.1523).
- 1304 [18] N. S. Amelin et al. "Collectivity in ultrarelativistic heavy ion collisions". In:
 1305 *Nucl. Phys. A* 544 (1992), p. 463. doi: [10.1016/0375-9474\(92\)90598-E](https://doi.org/10.1016/0375-9474(92)90598-E).
- 1307 [19] L. V. Bravina et al. "Fluid dynamics and Quark Gluon string model - What
 1308 we can expect for Au+Au collisions at 11.6 AGeV/c". In: *Nucl. Phys. A* 566
 1309 (1994), p. 461. doi: [10.1016/0375-9474\(94\)90669-6](https://doi.org/10.1016/0375-9474(94)90669-6).
- 1310 [20] L. V. Bravin et al. "Scaling violation of transverse flow in heavy ion colli-
 1311 sions at AGS energies". In: *Phys. Lett. B* 344 (1995), p. 49. doi: [10.1016/0370-2693\(94\)01560-Y](https://doi.org/10.1016/0370-2693(94)01560-Y).
- 1313 [21] B. Andersson et al. "A model for low-pT hadronic reactions with general-
 1314 izations to hadron-nucleus and nucleus-nucleus collisions". In: *Nucl. Phys.*
 1315 *B* 281 (1987), p. 289. doi: [10.1016/0550-3213\(87\)90257-4](https://doi.org/10.1016/0550-3213(87)90257-4).
- 1316 [22] B. Andersson, A. Tai, and B.-H. Sa. "Final state interactions in the (nuclear)
 1317 FRITIOF string interaction scenario". In: *Z. Phys. C* 70 (1996), pp. 499–
 1318 506. doi: [10.1007/s002880050127](https://doi.org/10.1007/s002880050127).
- 1319 [23] B. Nilsson-Almqvist and E. Stenlund. "Interactions Between Hadrons and
 1320 Nuclei: The Lund Monte Carlo, Fritiof Version 1.6". In: *Comput. Phys. Com-*
 1321 *mun.* 43 (1987), p. 387. doi: [10.1016/0010-4655\(87\)90056-7](https://doi.org/10.1016/0010-4655(87)90056-7).
- 1322 [24] B. Ganhuyag and V. Uzhinsky. "Modified FRITIOF code: Negative charged
 1323 particle production in high energy nucleus nucleus interactions". In: *Czech.*
 1324 *J. Phys.* 47 (1997), pp. 913–918. doi: [10.1023/A:1021296114786](https://doi.org/10.1023/A:1021296114786).
- 1325 [25] ATLAS Collaboration. "Topological cell clustering in the ATLAS calorime-
 1326 ters and its performance in LHC Run 1". In: (2016). arXiv: [1603.02934](https://arxiv.org/abs/1603.02934)
 1327 [*hep-ex*].
- 1328 [26] Peter Speckmayer. "Energy Measurement of Hadrons with the CERN AT-
 1329 LAS Calorimeter". Presented on 18 Jun 2008. PhD thesis. Vienna: Vienna,
 1330 Tech. U., 2008. URL: <http://cds.cern.ch/record/1112036>.

- 1331 [27] CMS Collaboration. “The CMS barrel calorimeter response to particle
1332 beams from 2 to 350 GeV/c”. In: *Eur. Phys. J. C* 60.3 (2009). doi: [10.1140/epjc/s10052-009-0959-5](https://doi.org/10.1140/epjc/s10052-009-0959-5).
- 1334 [28] J. Beringer et al. (Particle Data Group). “Review of Particle Physics”. In:
1335 *Chin. Phys. C* 38 (2014), p. 090001. URL: <http://pdg.lbl.gov>.
- 1336 [29] P. Adragna et al. “Measurement of Pion and Proton Response and Lon-
1337 gitudinal Shower Profiles up to 20 Nuclear Interaction Lengths with the
1338 ATLAS Tile Calorimeter”. In: *Nucl. Instrum. Meth. A* 615 (2010), pp. 158–
1339 181. doi: [10.1016/j.nima.2010.01.037](https://doi.org/10.1016/j.nima.2010.01.037).
- 1340 [30] ATLAS Collaboration. “Jet energy measurement and its systematic uncer-
1341 tainty in proton–proton collisions at $\sqrt{s} = 7$ TeV with the ATLAS detec-
1342 tor”. In: *Eur. Phys. J. C* 75 (2015), p. 17. doi: [10.1140/epjc/s10052-014-3190-y](https://doi.org/10.1140/epjc/s10052-014-3190-y). arXiv: [1406.0076 \[hep-ex\]](https://arxiv.org/abs/1406.0076). PERF-2012-01.
- 1344 [31] Hung-Liang Lai, Marco Guzzi, Joey Huston, Zhao Li, Pavel M. Nadolsky,
1345 et al. “New parton distributions for collider physics”. In: *Phys. Rev. D* 82
1346 (2010), p. 074024. doi: [10.1103/PhysRevD.82.074024](https://doi.org/10.1103/PhysRevD.82.074024). arXiv: [1007.2241 \[hep-ph\]](https://arxiv.org/abs/1007.2241).
- 1348 [32] E. Abat et al. “Study of energy response and resolution of the ATLAS barrel
1349 calorimeter to hadrons of energies from 20 to 350 GeV”. In: *Nucl. Instrum.*
1350 *Meth. A* 621.1-3 (2010), pp. 134 –150. doi: <http://dx.doi.org/10.1016/j.nima.2010.04.054>.
- 1352 [33] ATLAS Collaboration. “Jet energy measurement with the ATLAS detector
1353 in proton–proton collisions at $\sqrt{s} = 7$ TeV”. In: *Eur. Phys. J. C* 73 (2013),
1354 p. 2304. doi: [10.1140/epjc/s10052-013-2304-2](https://doi.org/10.1140/epjc/s10052-013-2304-2). arXiv: [1112.6426 \[hep-ex\]](https://arxiv.org/abs/1112.6426). PERF-2011-03.
- 1356 [34] ATLAS Collaboration. “Search for heavy long-lived charged R -hadrons
1357 with the ATLAS detector in 3.2 fb^{-1} of proton–proton collision data at
1358 $\sqrt{s} = 13$ TeV”. In: *Phys. Lett. B* 760 (2016), pp. 647–665. doi: [10.1016/j.physletb.2016.07.042](https://doi.org/10.1016/j.physletb.2016.07.042). arXiv: [1606.05129 \[hep-ex\]](https://arxiv.org/abs/1606.05129).
- 1360 [35] A. C. Kraan, J. B. Hansen, and P. Nevski. “Discovery potential of R-hadrons
1361 with the ATLAS detector”. In: *Eur. Phys. J. C* 49 (2007), pp. 623–640. doi:
1362 [10.1140/epjc/s10052-006-0162-x](https://doi.org/10.1140/epjc/s10052-006-0162-x). arXiv: [hep-ex/0511014 \[hep-ex\]](https://arxiv.org/abs/hep-ex/0511014).
- 1364 [36] K. A. Olive et al. “Review of Particle Physics”. In: *Chin. Phys. C* 38 (2014),
1365 p. 090001. doi: [10.1088/1674-1137/38/9/090001](https://doi.org/10.1088/1674-1137/38/9/090001).
- 1366 [37] “dE/dx measurement in the ATLAS Pixel Detector and its use for particle
1367 identification”. In: (2011).
- 1368 [38] ATLAS Collaboration. “The ATLAS Simulation Infrastructure”. In: *Eur.*
1369 *Phys. J. C* 70 (2010), pp. 823–874. doi: [10.1140/epjc/s10052-010-1429-9](https://doi.org/10.1140/epjc/s10052-010-1429-9). arXiv: [1005.4568 \[physics.ins-det\]](https://arxiv.org/abs/1005.4568).

- ¹³⁷¹ [39] ATLAS Collaboration. “Search for metastable heavy charged particles with
¹³⁷² large ionisation energy loss in $p\bar{p}$ collisions at $\sqrt{s} = 8$ TeV using the AT-
¹³⁷³ LAS experiment”. In: *Eur. Phys. J. C* 75 (2015), p. 407. doi: [10.1140/epjc/s10052-015-3609-0](https://doi.org/10.1140/epjc/s10052-015-3609-0). arXiv: [1506.05332 \[hep-ex\]](https://arxiv.org/abs/1506.05332). SUSY-
¹³⁷⁴ 2014-09.
¹³⁷⁵

1376 DECLARATION

1377 Put your declaration here.

1378 *Berkeley, CA, September 2016*

1379

Bradley Axen

1380

1381 COLOPHON

1382

Not sure that this is necessary.